

Tip-Enhanced Raman Imaging and Nanospectroscopy: Sensitivity, Symmetry, and Selection Rules

Catalin C. Neacsu · Samuel Berweger ·
Markus B. Raschke

Published online: 25 February 2009
© Humana Press Inc. 2009

Abstract The fundamental mechanisms of tip-enhanced Raman spectroscopy (TERS) have been investigated, including the role of the plasmonic excitation of the metallic tips, the nature of the optical tip-sample coupling, and the resulting local-field enhancement and confinement responsible for ultra-high resolution imaging down to just several nanometers. Criteria for the distinction of near-field signature from far-field imaging artifacts are addressed. TERS results of molecules are presented. With enhancement factors as high as 10^9 , single-molecule spectroscopy is demonstrated. Spatially resolved vibrational mapping of crystalline nanostructures and determination of crystallographic orientation and domains is discussed making use of the symmetry properties of the tip scattering response and the intrinsic Raman selection rules.

Keywords tip-enhanced Raman imaging · nanospectroscopy · tip-enhanced Raman spectroscopy

Introduction

Optical spectroscopy provides nondestructive techniques for obtaining both structural and real-time dynamic information of molecules and solids. Vibrational spectroscopy in particular, by directly coupling to the nuclear motion, offers insight into chemical

composition, molecular bonds, intermolecular coupling, and zone-center phonons in crystalline solids [1, 2]. IR and Raman spectroscopy provide complementary information. Raman spectroscopy features fewer constraints in terms of selection rules, readily provides access to low frequency vibrations [3–6], and is carried out in the visible to near IR spectral range in a comparably simple experimental design. However, with scattering cross-sections of $\sim 10^{-27} - 10^{-30} \text{ cm}^2$, the Raman response is weak, generally requiring probing a large molecular ensemble or bulk solids [7, 8].

It is therefore desirable to combine the intrinsic chemical specificity of Raman spectroscopy with optical microscopy for the investigation of the spatial heterogeneity and composition of the analyte. In that regard, the optical far-field Raman microscope has become an established tool for material characterization on the micrometer scale and in a confocal implementation with spatial resolution down to several hundred nanometers [9]. However, for most applications, the desired spatial resolution often exceeds the resolution imposed by far-field diffraction [10, 11].

Scanning near-field optical microscopy (SNOM) provides access to subwavelength scale spatial resolution [12–19]. Aperture-based SNOM using tapered glass fiber tips has been employed for nano-Raman spectroscopy [20–23]. However, the low optical throughput of the aperture probes ($10^{-3} - 10^{-5}$) severely limits the spatial resolution and the sensitivity that can be obtained, resulting in a long imaging time and parasitic Raman signal from the glass tip that could be an impediment [22].

High sensitivity in Raman scattering, in general, can be achieved by surface-enhanced Raman spectroscopy (SERS), providing a strongly enhanced Raman

C. C. Neacsu (✉) · S. Berweger · M. B. Raschke
Department of Chemistry, University of Washington,
Seattle, WA 98195-1700, USA
e-mail: neacsu@u.washington.edu

response from molecular adsorbates on rough metallic surfaces or colloidal aggregates [24–26]. SERS is due to the near-field enhancement of the electromagnetic field at single or coupled metal nanostructures often resonantly excited at their surface plasmon polariton (SPP) eigenmodes [27–34]. Together with a corresponding but weaker ($\sim 10^1$ – 10^2) chemical contribution [35] originating from surface bonding or charge transfer, the electromagnetic enhancement leads to a total increase in Raman signal by up to 14 orders of magnitude, allowing for detection down to the single molecule level [36–41]. Despite its potential for chemically specific detection of minute amounts of analytes, it has remained challenging to develop SERS into a routine analytic spectroscopic tool mostly due to difficulties associated with the reproducible fabrication of SERS-active substrates [42–45].

Better control over the SERS active sites and their field enhancement can be achieved by what may be viewed as resorting to an inverse geometry with respect to SERS: suspension of the metal nanostructure providing the field enhancement at a small distance above the analyte [46]. This is the basis of tip-enhanced Raman scattering (TERS) making use of a single plasmon-resonant metallic nanostructure provided in the form of a scanning probe tip of suitable material and geometry.

Fundamentally, TERS is a variant of scattering-type scanning near-field optical microscopy (*s*-SNOM) [47–51]. All-optical resolution down to just several nanometers is provided by *s*-SNOM, in the visible [52–54] and IR spectral regions [55–58]. TERS is the extension of this technique to inelastic light scattering with the metallic tip used as an active probe, which provides both the local-field enhancement and serves as an efficient scatterer for the Raman emission.

s-SNOM and special aspects of TERS have been addressed in recent reviews [18, 19, 59–62] (and references therein), but no comprehensive discussion of the underlying physical mechanisms has yet been provided. Here, we review our recent contributions to the understanding of near-field Raman enhancement and sensitivity, tip-sample coupling, spatial resolution, the importance of the plasmonic character of the tip, and tip fabrication. In addition, we show that the symmetry properties of the tip-scattering geometry in combination with the Raman selection rules allows for the determination of crystallographic information on the nanoscale. This, together with the results of other groups, shows the potential of TERS as a nanoanalytical tool with diverse applications in material and surface science and analytical chemistry for the study of biomolecular interfaces, molecular adsorbates, nanostructures, and nanocomposites.

Tip-Enhanced Raman Spectroscopy

TERS combines the advantages of SERS with those offered by *s*-SNOM: the single nanoscopic tip apex provides the local field enhancement at a desired sample location without requiring any special sample preparation [63, 64]. With the spatial resolution mainly limited by the tip apex size, chemical analysis on the nanometer scale is made possible. By raster scanning the sample, spatially resolved spectral Raman maps with nanometer resolution can be obtained simultaneously with the topography in atomic force microscopy (AFM) or surface electronic properties in scanning tunneling microscopy (STM).

The origin of the field enhancement at the tip apex is attributed to the singular behavior of the electromagnetic field (akin to the lightning-rod effect). In addition, the spatial confinement allows for the possible excitation of localized SPPs (tip-plasmons) for certain tip materials [65]. With the first effect being geometrical in origin, its magnitude is mainly dependent on the curvature of the apex. Taking advantage of the excitation of tip-plasmons can further increase the overall enhancement by several orders of magnitude, as will be discussed further on.

Ultra-high sensitivity and nanometer spatial resolution imaging using TERS were obtained on various materials and molecular systems adsorbed on both flat and corrugated surfaces [66–85]. Having large Raman cross-sections, several dye molecules (e.g., malachite green (MG), rhodamine 6G, brilliant cresyl blue) were used and near-field Raman enhancement factors up to $\sim 10^9$ were achieved [68, 71, 77, 81, 82]. Using Ag-coated AFM tips, spatial resolution below 50 nm was obtained on surface layers of Rhodamine 6G dye molecules [68, 71]. Lateral resolution as high as 14 nm and a maximum Raman enhancement factor estimated at $\sim 10^4$ were obtained in spatially resolved probing vibrational modes along individual carbon nanotubes [72, 73, 78].

In studies of adenine, as well as C_{60} molecules, the tip-induced mechanical force was shown to lead to mechanical strain-induced frequency shifts of the normal Raman modes [74, 80]. Furthermore, it was observed that, when interacting with individual metal atoms of the tip apex, adenine molecules form different isomers, demonstrating the potential for TERS to have for atomic site selective sensitivity [83].

Extension of TERS implementation for coherent spectroscopy was shown for coherent anti-Stokes Raman scattering (CARS) of adenine molecules included in a DNA network [75]. Owing to the third-order nonlinearity of the CARS process, the induced

polarization at the tip apex is further confined, and higher lateral resolution is, in principle, possible [76]. Concomitant, theoretical studies on TERS report field enhancements up to three orders of magnitude in particular wavelength regions [86–91]. However, the expected resulting TERS enhancement of 12 orders of magnitude has not yet been observed experimentally.

In recent work from our group, we have refined the metallic tip fabrication and experimentally identified and theoretically discussed the importance of the plasmonic properties of the scanning tip to achieve high Raman sensitivity [92–95]. This has enabled near-field Raman enhancement factors of up to 10^9 from MG molecules adsorbed on smooth Au surfaces to be obtained, allowing for the detection of TERS response with single molecule sensitivity [81, 96].

The review is organized as follows: The experimental arrangement is presented in the “[Experimental](#)” section. This includes laser excitation, Raman detection, metallic tip fabrication by electrochemical etching, and molecular systems used. “[Optical Tip Characterization](#)” discusses the experimental characterization of the optical properties of the tips including their plasmonic behavior and the local-field enhancement factor as determined by second harmonic generation (SHG). “[Calculation of the Near-Field Distribution at the Tip-Apex](#)” describes the theoretical analysis of the near-field distribution at the tip apex together with its spectral characteristics. The tip-sample optical coupling is discussed in the “[Optical Tip-Sample Coupling](#)” section, where its effect on sensitivity, spatial resolution, and spectral shift of the plasmon resonance are derived. The near-field character vs far-field imaging artifacts in TERS and its polarization dependence are addressed in the “[Near-Field Character and Far-Field Artifacts in TERS](#)” section. The procedure for estimating the near-field enhancement factor is detailed and representative values discussed. Tip-enhanced near-field spectra of monolayer (ML) and a submonolayer of molecular adsorbates on a smooth Au surface are given in the “[TERS of Molecular Adsorbates](#)” section. The high sensitivity obtained and the dependence of the spectral features on the enhancement level is discussed. In the “[Molecular Bleaching](#)” section, we also address the important question of molecular bleaching and possible chemical contamination paths and show a number of control experiments. Near-field tip-enhanced Raman results with single molecule sensitivity are shown in the “[TERS with Single Molecule Sensitivity](#)” section. This is concluded from the ultra-low molecular coverage and the observed intensity and spectral temporal fluctuations. We identify and propose in the “[Raman](#)

[Imaging of Nanocrystals: Near-Field Crystallographic Symmetry](#)” section a new and promising extension of TERS for determination of both chemical and structural properties of nanocrystals. The “[Outlook](#)” section gives an outlook on TERS, and novel ways to circumvent current instrumental difficulties are discussed.

Experimental

Various experimental schemes have been employed for TERS experiments. A tip axial illumination and detection geometry has been used, allowing for high numerical aperture (NA), but requiring transparent samples or substrates [73, 97]. A high-NA parabolic mirror can be used to probe nontransparent samples [98, 99]. In both schemes, the tip is illuminated along the axial direction with the tip apex positioned in the laser focus. For these geometries, polarization conditions require either a Hermite–Gaussian beam [100] or radial incident polarization [98, 101]. While allowing for efficient excitation and detection with the tip, independent polarization and k-vector control is limited but desirable for symmetry selective Raman probing.

In contrast, side-on illumination and detection allows for greater flexibility in the selection of polarization and k-vector, as well as the use of nontransparent samples. The scanning and tip-sample distance are controlled using either an atomic force microscope (AFM) or a scanning tunneling microscope (STM), with STM restricted to the use of conducting samples.

Figure 1 shows the experimental layout of our side-illuminated TERS experiment. The incident radiation (ν_i) is focused onto the tip-sample gap and the tip-scattered Raman light (ν_s) is detected. For the experiments described here, a shear-force AFM is used. Shear-force AFM maintains a constant height of several nanometers above the sample. Due to the short-range tip-sample distance dependence of the optical field enhancement, dynamic noncontact AFM is less suitable. The time-averaged signal is greatly reduced due to the oscillating tip. Contact AFM maintains a constant and small tip-sample distance but the comparably large forces make it unfavorable for probing molecular or soft matter samples. In contrast, with the spatial range of shear-forces confined to within 25 nm [102], the shear-force AFM tip is controlled in close proximity to the sample without actual physical contact.

The control mechanism in shear-force AFM is based on the near surface vibrational damping of a probe tip oscillating parallel to the surface. The nature of the shear-force damping mechanism is not yet fully

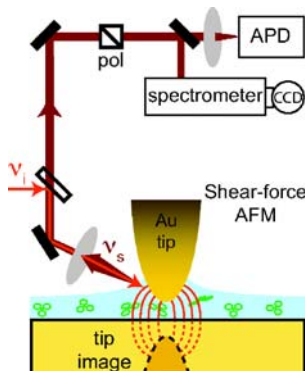


Fig. 1 Schematic of the experimental arrangement for TERS. The incident light is focused onto the tip-sample gap. The tip-enhanced and -scattered Raman response is spectrally filtered using a notch filter and is spectrally resolved by an imaging spectrometer with a liquid nitrogen-cooled charge-coupled device array, or integrally detected by means of an avalanche photodiode (*APD*). Polarization directions of both incident and scattered light beams can be controlled independently. The *blue layer* indicates a thin water film as may be present on the sample under ambient conditions.

understood [19], with a variety of mechanisms being discussed [103–106]. It has been suggested [107, 108] that the tip experiences viscous damping from a thin water layer adsorbed on the surface of the sample under ambient conditions [108–110]. This water layer, present on most hydrophilic samples, may play an important role in the surface diffusion of the analyte molecules and possibly the transition of molecules to adsorb onto the tip.

For an incident light source, a continuous wave Helium–Neon laser, with $\lambda_i = 632.8$ nm (1.92 eV) is commonly used [2]. In our experiments, after passing through a laser-line filter, the light is focused onto the tip-sample gap by means of a long working distance microscope objective (NA = 0.35). The tip-backscattered light is collected with the same objective and spectrally filtered using a notch filter. The signal is detected using either an avalanche photodiode or spectrally resolved using a fiber-coupled imaging spectrograph with a liquid nitrogen-cooled charge-coupled device detector. Even for large enhancements, the signal intensities are weak, and detector noise is one limiting factor. We therefore limit the spectral resolution to 25 cm^{-1} for the tip-enhanced experiments. Far-field spectroscopic studies of molecular MLs serving as reference to quantify the enhancement are conducted using a micro-Raman confocal setup, based on an inverted microscope (Zeiss Axiovert 135).

For our experiments, we chose MG, an organic triphenylmethane laser dye with an absorption peak around $\lambda \approx 635$ nm. The absorption peak of MG is very close

to the laser energy used, leading to a resonant Raman excitation via the S_0 – S_1 electronic transition of the conjugated π -electron system, as discussed below [111]. To limit the rate of the molecular decomposition, the maximum fluence in the focus of the microscope objective was $5 \times 10^3 - 3 \times 10^4$ W/cm^2 . However, molecular bleaching prevails under ambient conditions under resonant Raman excitation in TERS [81, 112].

Tip Fabrication

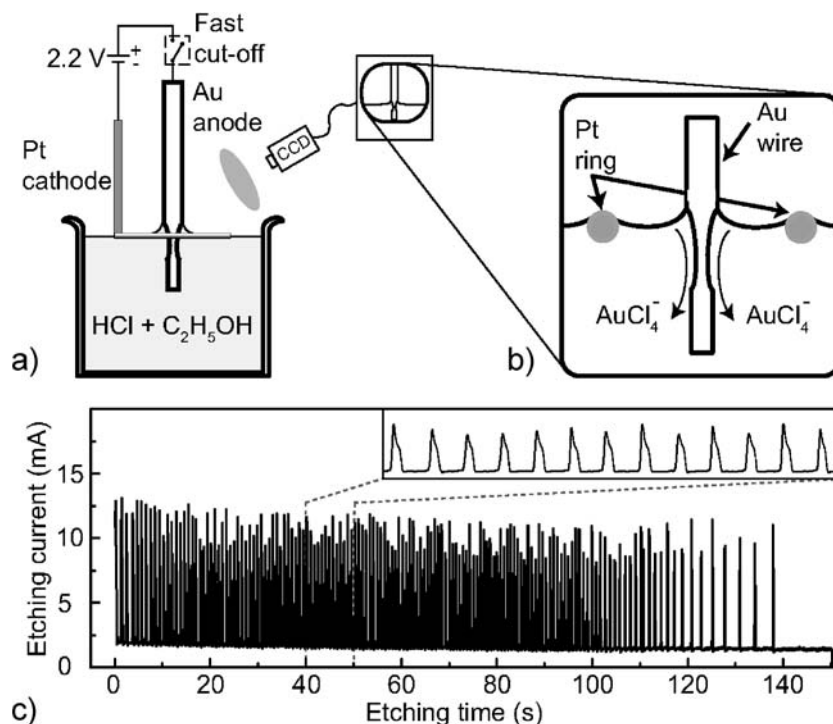
The metallic scanning probe tips hold the central function in TERS studies, providing the enhanced electromagnetic field at their apex. Ideally, as discussed below, they present strong plasmon resonances in the spectral region of interest, leading to enhanced pump (ν_i) and scattered Raman fields (ν_s) at the apex. Since the first experiments, the fabrication of suitable tips has been a major experimental challenge. A variety of methods for their fabrication have been used: including angle-cutting the metal wire [113], DC or AC voltage electrochemical and milling procedures [114–117], focused ion beam milling [54], metal-coating commercially available cantilever AFM tips [118, 119], and attaching spherical or other plasmonic nanoparticles to a glass tip [120]. Electrochemical etching [98, 121] is most commonly used due to perceived advantages [122] of tips fabricated in this manner.

We employ a DC voltage electrochemical etching method for both Au and W tips. It involves the anodic oxidation of the metal wire [123]. In the case of Au, it involves the formation of soluble AuCl_4^- , which subsequently diffuses away from the electrode [121].

The schematic of the electrochemical cell used is depicted in Fig. 2a. After careful cleaning with acetone, the Au wire ($\phi = 0.125$ mm, purity 99.99%, temper as drawn, Advent Research Materials) is partially immersed (~ 2 – 3 mm) into the electrolyte solution. As an electrolyte, a 1:1 mixture of hydrochloric acid (HCl, aq. 37%) and ethanol is used. As cathode, a platinum wire ($\phi = 0.3$ mm) circular ring electrode with a diameter of ~ 1 cm is utilized. It is held at the surface of the electrolyte with the Au wire positioned at the center of the Pt ring. For the etching, a potential of +2.2 V is applied to the Au anode with respect to the Pt cathode. This voltage was determined by us, as well as others [124], to produce the best tips. This value is well above the Au oxidation potential due in part to the activation energy along the reaction pathway [114].

When placed in the electrolyte solution, the surface tension causes a concave meniscus to form around the wire, as shown schematically in Fig. 2b. The overall shape and aspect ratio of the tip after etching are

Fig. 2 Schematics of the electrochemical etching cell. **a** The Au wire (anode) is partially immersed into the electrolyte solution. It is surrounded by the Pt-ring cathode. The evolution of the etching process is closely followed using a video microscope. **b** The etching takes place at the meniscus formed around the Au-wire. The flow of AuCl_4^- is shown. For W-tips, a similar procedure is used (see text). **c** Time evolution of the etching current for a potential of 2.2 V. The current oscillations are periodic for about 100 s, after which they become less frequent, although they maintain the amplitude. For periodic current oscillations (*inset*), tips with smooth surface and consistent taper are obtained.



primarily determined by the shape of the meniscus [121]. During etching, a downward flow of AuCl_4^- along the wire can be observed. The resulting ion concentration gradient partially inhibits etching of the lower portion of the wire, resulting in a necking of the wire near the meniscus [125]. This proceeds until the lower section of the wire falls off. The remaining upper part of the wire is then used as a TERS/AFM tip.

Since the tip remains in the solution under the meniscus after the detachment of the lower part, the circuit has to switch off as rapidly as possible, as further etching would result in blunt tips. A comparator breaks the etching voltage when the current value becomes smaller than an adjustable reference value determined from the current change associated with the drop of the lower tip.

Monitoring the etching current reveals periodic oscillations of the current, as is shown in Fig 2c. For the potential of 2.2 V, the etching will generally reach completion in approximately 150 s with an average baseline current of ~ 2 mA. After a short time of initial fluctuations, the period equilibrates and remains constant for the first ~ 100 s of the etching duration. Towards the end of the etching process, the oscillation period continuously decreases until completion.

These current oscillations have been attributed to the depletion of Cl^- near the surface of the electrode [121]. Initially, the Au will react rapidly to form AuCl_4^- , depleting the Cl^- near the electrode–

electrolyte interface and resulting in a period of high current. With decreasing local Cl^- concentration, the Au will more readily form an electrode-passivating layer of $\text{Au}(\text{OH})_3$ [126], leading to extended periods of decreased current. Upon restoration of the local Cl^- concentration, the passivating layer dissolves and another current spike occurs [127]. The details of this oscillating electrochemical process are sensitively dependent on the applied potential. An empirically established etching voltage leads to the most periodic oscillations and results in the highest quality tips.

It is desirable to have a criterion to select suitable TERS tips other than scanning electron microscopy (SEM) which is known to deposit Raman-visible carbon contamination onto the tips due to electron-beam induced decomposition of trace organics in the residual gas [128, 129]. Tips etched under a constant oscillation period exhibit a smooth surface and consistent taper. In contrast, tips etched with an irregular periodicity of the etching current frequently present deformities and large surface irregularities. We could verify in our experiments a link between homogeneous and smooth taper with TERS performance by comparison of TERS activity with SEM of tip shape as well as the study of SPP of the tip apex. Our observations here are in good agreement with previous work by Wang et al. [124].

A similar etching procedure is used for the tungsten tips. A W wire ($\phi = 200 \mu\text{m}$) is partially immersed ($\sim 2\text{--}3$ mm) in aqueous 2 M KOH. A DC voltage of 3 V

is applied between the wire and a stainless steel ring cathode. Using these procedures, tips with apex radii as small as 10 nm are obtained. After etching, the tips are cleaned in distilled water and stored in isopropanol prior to usage to avoid possible contamination in an otherwise uncontrolled atmosphere.

Optical Tip Characterization

Efficient local-field enhancement and TERS activity is, in general, associated with the excitation of local modes of SPPs at the metallic tip [63, 73, 130–132]. However, determining the details of this correlation has remained an open problem. In the following section, we present the investigation of the spectral characteristics of the elastic light scattering from individual sharp metal tips and discuss the results in the context of the local plasmonic resonant behavior.

SPPs of Au Tips

Dark-field scattering spectroscopy with white light illumination would lead to a largely unspecific response with the scattering dominated by the tip shaft [133], and the SPP characteristics of the apex itself would become difficult to distinguish.

Therefore, for the plasmonic light tip-scattering experiments, we spatially limit the optical excitation to the near-apex region by use of evanescent wave excitation. For that purpose, the tip frustrates the evanescent field formed by total internal reflection on a prism base [134, 135], and the tip-scattered light is detected and spectrally analyzed. This confines the excitation to just several 100 nm from the tip apex. The complete description of the setup and the results are given elsewhere [93].

Figure 3 shows representative scattering spectra for different Au (a, b) and W (c, d) tips. Both the excitation and detected light fields are unpolarized. All spectra are acquired for the tips within a few nanometers above the prism surface, as controlled by shear-force AFM. The intensity scale is the same for all four cases, and the spectra are offset for clarity. Electron micrographs for the tip structures investigated are shown as insets.

The pronounced wavelength dependence of the scattering of Au tips is characteristic of a plasmon resonant behavior. Both scattering intensity and spectral position of the resonance are found to be sensitive to the structural details of the tips. In general, for regular tip shapes, the resonance is characterized by one (Fig. 3a) distinct spectral feature. Inhomogeneities in the geo-

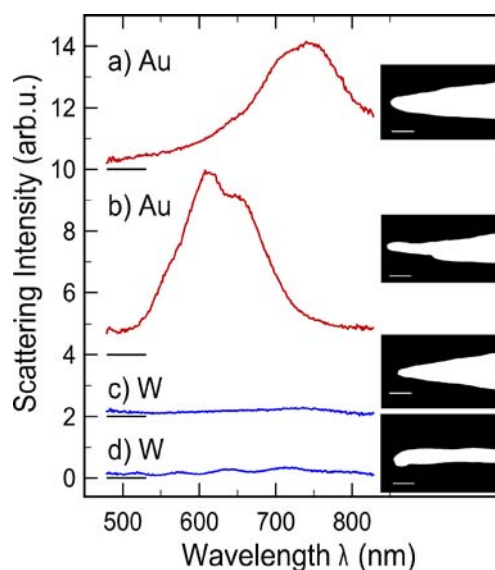


Fig. 3 Scattering spectra for different Au and W tips. A plasmon-resonant behavior is observed for Au tips (a, b). Weaker and, in general, spectrally flat signals are observed in the case of W tips (c, d). The spectral data are juxtaposed with the electron microscope image from the corresponding tip. The scale bar corresponds to 100 nm [93].

metric shape are reflected in spectral broadening and/or occurrence of multiple spectral features (Fig. 3b). In addition, the spectral position and shape of the plasmon resonance depend sensitively on the aspect ratio of the tip.

For comparison, spectral light scattering by tungsten tips of similar dimensions is shown in Fig. 3c and d. Overall weaker emission intensities are observed compared to Au tips. For W, a metal with strong polarization damping due to absorptive loss in the visible and near-IR region, no SPP resonance is expected. Here, a spectrally flat optical response is observed with weak overall scattering intensities (Fig. 3c). The spectral behavior is found to show little variation with tip radius and tip cone angle, except for the case of very slender tips, where a modulation is observed as shown in Fig. 3d.

From polarization-dependent studies of the tip scattering process, we have found that more intense scattering is observed for emission polarized parallel with respect to the tip axis (*p*-polarized emission), corresponding to the excitation of longitudinal plasmonic modes. The intensity ratio of *p* to *s* (emission orthogonal to the tip axis) is typically found to range between 2 and 5, with a maximum value of ~ 10 . In the context of the TERS experiments, it must be noted that the *s*-polarized field is not expected to be enhanced near a surface. In this case, the optical

polarization of the tip and the corresponding image polarization induced in the sample are oriented antiparallel, as will be discussed in the “[Optical Tip–Sample Coupling](#)” section.

Local-Field Enhancement from Bare Tips

The highly resonant characteristics observed for Au tips suggest strong local-field enhancements in the vicinity of the apex. The quantification of the near-field enhancement factor is a difficult task in general. Without an absolute reference, the enhancement factor cannot readily be quantified from linear optical experiments. We therefore make use of the symmetry selectivity of the second-order nonlinear optical response in the form of SHG from the apex region of the tips.

SHG is forbidden in the dipole approximation for media with inversion symmetry [136]. In scattering geometry for sagittal illumination and tip-parallel polarization, the SHG response from the tip is dominated by the apex region where the macroscopic translational invariance is broken in the axial direction. With the symmetry being radially conserved, little signal is expected from the conical near-apex shaft area.¹ For the experiments, linearly polarized incident light from a mode-locked Ti:sapphire oscillator (pulse duration < 15 fs, $\lambda = 805$ nm) is directed onto the sharp end of the free standing tip and the scattered SHG signal is spectrally selected and detected.

The contribution of the local field-enhancement of SHG from the metal tips is derived by comparing the signal strength obtained to that of a planar surface of the same material. With the SH-enhancement expected to be dominated by the tip apex, a SH-enhancement of $\sim 5 \times 10^3 - 4 \times 10^4$ was observed for Au tips with $r \simeq 20$ nm. For a SH-power $\propto E^4$ [137], this corresponds to an amplification of 8–25 for the average electric field near the apex, in agreement with estimates based on other SHG experiments [138]. For W tips, significantly lower values for the SH enhancement are found corresponding to local field factors between 3 and 6. These results are also in good agreement with theoretical models despite microscopic variations in the details of the tip geometry.

The excitation of the localized SPP in the axial direction is responsible for the field enhancement observed

¹In addition to the unique symmetry properties, the local surface and nonlocal longitudinal bulk polarizations contributions to the nonlinear polarization and their directional and polarization selection rules are directly distinguishable here due to the geometry of the tip as a partial asymmetric (∞mm) nanostructure with the mirror symmetry broken along the axis.

experimentally for Au tips. A systematic investigation of the influence of these geometric parameters in terms of cone angle and tip radius would be highly desirable; however, the limitations due to the electrochemical preparation procedure render this difficult.

Calculation of the Near-Field Distribution at the Tip-Apex

The near-field distribution and enhancement have been derived theoretically for a variety of tip model geometries and tip and sample material combinations using different theoretical methods [81, 92, 95, 130, 132, 139–142] (and references therein). The accurate theoretical treatment of the problem involves the solutions of Maxwell’s equations. This can be performed numerically for a chosen model tip-geometry [94, 131, 143, 144]. Although this may closely reproduce the experimental observations, the approach is computationally very demanding. In addition, it has remained difficult to extract the underlying relevant microscopic parameters responsible for the optical response observed given that the effects of tip geometry, tip material, tip–sample distance, and optical field are coupled.

Taking advantage of the small dimensions of the tip apex compared to the optical wavelength ($kr \ll 1$, with k the wave vector and r the tip-apex radius), the problem can be treated in the quasistatic approximation, which allows solving the Laplace equation analytically for certain geometries [95, 130, 132, 140–142] to derive the local field distribution [87, 145]. For a size of the apex region of $r \sim 10$ nm, this implies that the electric field has the same amplitude and phase across the structure at any time; thus, retardation effects can be neglected [133, 146]. Despite constraints in terms of the tip geometries that can be treated in this approach (paraboloidal, spheroidal, hyperboloidal), this method provides direct insight into how the solutions scale with several experimentally relevant structural and material parameters.

Here, we approximate the tip geometry as a hyperboloid. The influence of different dielectric and structural parameters on the near-field enhancement and distribution is systematically derived for both bare tips and tip–sample systems [95]. The optical wavelength dependence is explicitly taken into account considering the frequency dependence of the dielectric functions of tip and sample media [147].

The field distributions and enhancement and their spectral dependence calculated within the quasistatic approximation for a hyperbolical tip are found to agree with other detailed theoretical observations. Using a

fully 3D finite-difference time-domain method, we have calculated the field distribution [94] with results similar to those obtained in [140, 144, 148]. The comparison with both the exact theoretical treatments and experimental results validates the approach of treating the probe tip in the quasistatic approach to a good approximation. Despite the simplicity of the model, the essential optical properties and the physical trends characteristic for the optical response of the tip–sample system are accurately predicted.

Figure 4 shows characteristic local field distributions and the corresponding enhancement near the apex region of free standing tips of gold (a) and tungsten (b). The equipotential surfaces are indicated by solid lines. In both cases, the radius of the apex and the cone semiangle are fixed to $r = 10$ nm and to $\theta = 20^\circ$, respectively. This closely resembles the conditions in the TERS experiments by setting the incident light at a wavelength of $\lambda = 630$ nm and the polarization along the tip axis.

At optical frequencies, even for metallic tip material, the tip surface does not represent an equipotential in contrast to the pure electrostatic case. The finite response time of the charge carriers with respect to the optical frequency results in the decay of the field inside the tip on the length scale given by the skin depth. For gold as a representative material with high conductivity, this results in the strongest field enhancement

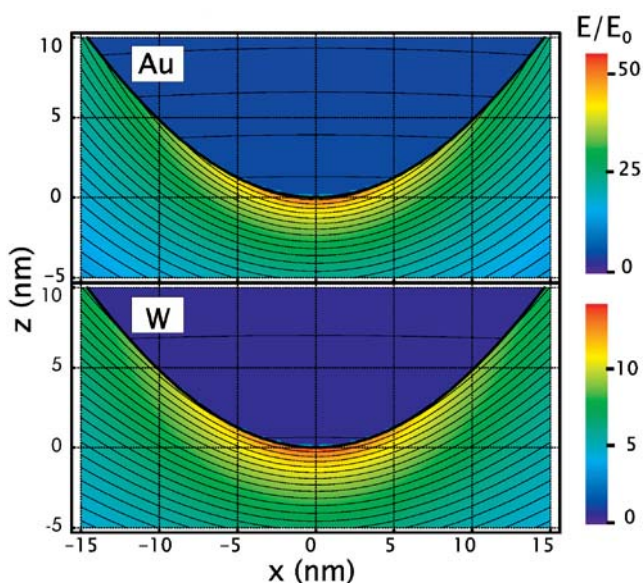


Fig. 4 Dependence of field enhancement (E/E_0) on tip material for free-standing Au and W tips with apex radius $r = 10$ nm, and wavelength of $\lambda = 630$ nm. The *solid lines* represent contours of constant potential [95].

of $E/E_0 \approx 50$ at the apex.² In contrast, tungsten is a poor conductor in the optical frequency range leading to a comparably moderate enhancement of ~ 12 . The degree of field enhancement E/E_0 at the tip apex depends sensitively on apex radius and cone semiangle due to their influence on the plasmon resonance, as discussed briefly below and in [95]. Typical values range between 10 and 100 for gold tips with 10–20 nm radius and realistic semiangles.

Despite the necessary approximations inherent to the quasistatic approach, the theoretical results presented here prove to be sufficiently accurate for most practical purposes. This is drawn from comparison of the field enhancement factors with the experimental results of the “Optical Tip Characterization” section. From the tip-scattered SHG experiments, the local field enhancement of 8–25 for Au and 3–6 for W was estimated for $r = 20$ -nm apex radii [92]. Considering that the experimental enhancement factors are obtained as a spatial average over the apex region, these values fall well within the range of the theoretically predicted enhancements given in Fig. 4.

Optical Tip–Sample Coupling

The local field enhancement, as well as the lateral confinement, can change significantly for the tip in close proximity to a surface plane. This behavior is of crucial importance for the optical contrast in scattering near-field microscopy. The optical tip–sample coupling is the result of the forcing of the boundary conditions at the surface plane on the field emerging from the apex. With the incident electric field inducing an optical dipole excitation in the tip, the presence of the sample can be accounted for by considering a virtual image dipole located inside the sample, with the resulting field distribution being a superposition of the fields of the two dipoles [149]. This gives rise to a mutual and constructive tip–sample optical polarization when the electric field is oriented parallel with respect to the tip axis (p -polarized). For an s -polarized incident field, the tip-dipole is induced parallel to the sample surface, and the correspondent image-dipole aligned antiparallel. This leads to a partial cancellation and reduced field intensity and scattering [58].

Figure 5 (top panel) displays the evolution of the field in the tip–sample gap calculated along the axial

²Note that for the calculations that refer to the field at the tip apex, the field is calculated at 0.125 nm below the apex to avoid numerical artifacts due to finite grid size.

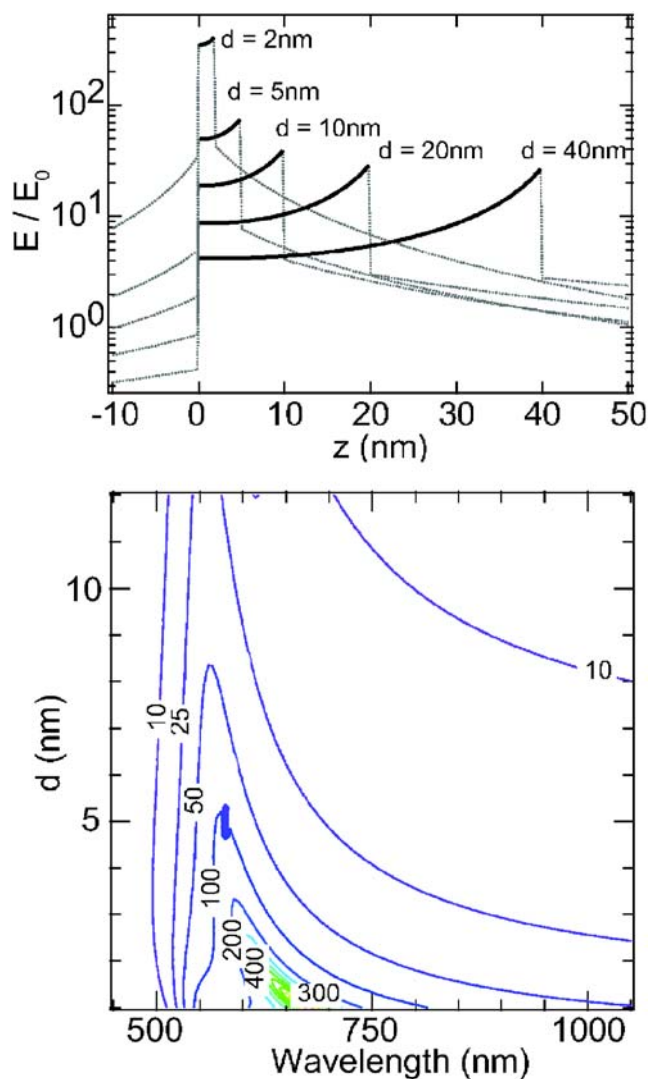


Fig. 5 *Top:* Variation of field enhancement E/E_0 along the axial direction across the tip-sample gap region for different distances d for an Au tip ($r = 10$ nm) and Au sample at an excitation wavelength of $\lambda = 630$ nm. The tip is at variable $z = d$ positions and extends to the right. The sample surface is located at $z = 0$ nm and its bulk occupies the range of negative z -values. *Bottom:* Spectral dependence of field-enhancement with tip-sample distance d for an Au tip ($r = 10$ nm) approaching an Au surface. The pronounced red shift of the plasmon response is associated with the strong near-field tip-sample coupling for $d \leq r$. The lines represent contours of equal optical field enhancement [95].

direction for different distances d for an Au tip approaching a flat Au sample. The tip-sample approach is accompanied by a significant increase in field enhancement in the tip-sample gap. The tip-sample interaction is correlated with apex radius and becomes significant at distances below about twice the tip radius (here, $d = 20$ nm). Here, the near-field interaction becomes effective with a particularly fast rise of the field at the

sample surface. The local field enhancement reaches values of up to several hundred for $d = 2$ nm, showing an increase of more than one order of magnitude when compared with the free-standing tip. In addition, the field enhancement with decreasing tip-sample distance is accompanied by a strong lateral confinement of the field underneath the apex [95]. The equipotential surface is forced to align nearly parallel with respect to the metallic substrate plane, which gives rise to an enhanced lateral concentration of the field. This is important, as it leads to an increased spatial resolution in scanning probe near-field microscopy for small tip-sample distances.

The details of the near-field distribution in the tip-sample gap depend on the optical properties of the tip and the sample materials that affect both field enhancement and lateral confinement. The lateral spatial resolution that can be obtained is determined by the near-field spatial extent and is given to the first order by the tip apex radius; however, deviations from this simple scaling behavior can be expected as the apex dimensions become smaller than the typical metal skin depth of ~ 20 – 25 nm at visible frequencies. In addition, the dielectric properties of both tip and sample determine the details of the field distribution in the gap region. In particular, the lateral confinement decreases with a decrease of the material optical polarizability, as discussed in [95]. Probing metallic samples with metallic tips at small tip-sample gaps results in the highest spatial resolution. In contrast, the lateral resolution will be lower when imaging dielectric surfaces in otherwise identical experimental conditions.

One of the virtues of the quasistatic model is the direct access to the spectral variation of the field enhancement and its distribution for different tip-sample geometries. The spectral tip-scattered response can become a complex superposition of the tip and the sample optical properties, the understanding of which is important in nanospectroscopy. Figure 5 (bottom panel) shows the calculated spectral dependence of the field enhancement near the surface for an Au tip ($r = 10$ nm) approaching an Au surface. As expected, a structural plasmon resonant behavior is observed. Associated with the increase in field enhancement for shorter distances a spectral shift in the plasmon response to longer wavelengths is observed. This red shift is especially pronounced for distances $d \leq r$, correlated with the onset of the sharp rise in field enhancement in the regime of strong coupling. It is the result of the superposition of the dielectric functions of the tip and the sample material mediated by the tip-sample optical coupling. This is a general phenomenon and it is found in calculations of spheres and other plasmonic nanostructures in close

proximity to metal surfaces [132, 144, 150, 151], and it has been observed experimentally in TERS and light emission in inelastic tunneling [152–154].

Predicted spectral peak widths of the order of 0.2 to 0.3 eV correspond to what is expected from the electronic dephasing times for SPP in Au of $\sim 4\text{--}7$ fs [155]. Using tungsten as tip material, no plasmon behavior is obtained except for the case when it is combined with a metallic sample that can itself sustain an SPP at the corresponding wavelength [95].

The determination of the field enhancement for a tip–sample coupled system has been experimentally achieved by TERS from surface MLs of molecular adsorbates [73, 77, 81, 85, 94]. From tip–sample distance-dependent Raman measurements in comparison with corresponding far-field experiments using MG dye molecules or single-walled carbon nanotubes, near-field enhancements of 60–150 at the sample surface were measured, as detailed below. These experimental values are in good agreement with the theoretical predictions, which range from ~ 50 to ~ 300 , as shown in Fig. 5 for small tip–sample distances.

Near-Field Character and Far-Field Artifacts in TERS

TERS manifests itself in an enhancement of the Raman response, with the increase confined to the region underneath the tip-apex. However, with the illumination extended on a larger surface region determined by the far-field focus, the discrimination of the variation of far-field response due to the presence of the tip inside the focus is difficult (Hartschuh et al. [73]).

Without any lateral scanning or systematic vertical tip–sample distance variations, this does not allow for the unambiguous assignment of the observed optical effect to a near-field process. The apparent Raman signal rise may be due to far-field effects associated with the tip being scanned inside the tight laser focus. This can influence both signal generation and detection. As the tip penetrates into the focus region, it would scatter additional otherwise forward-scattered (nonenhanced) far-field Raman light back into the detector. Furthermore, the interference of the tip-scattered and surface-reflected contributions with direct incident pump light results in locally enhanced pump intensities. With both processes affecting a surface region not confined by the apex area, near-field effects may be obscured by an increase in far-field signal.

In Fig. 6, tip-scattered Raman results are shown for single-wall carbon nanotubes and MLs of MG

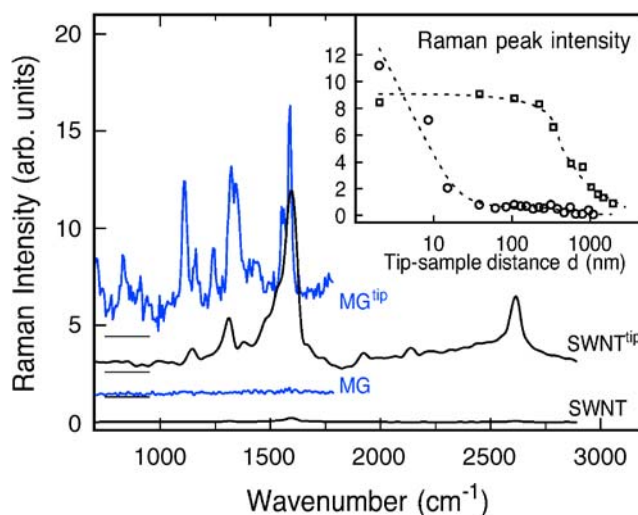


Fig. 6 Near-field signature vs far-field artifact: Raman spectra of single-walled carbon nanotubes and MG molecules with tip retracted ($SWNT$, MG) and tip engaged ($SWNT^{tip}$, MG^{tip}). *Inset*: tip–sample distance dependence of the Raman signal obtained under similar conditions but displaying very different behaviors: the ~ 20 -nm-length scale increase is characteristic for the near-field signal origin (circles); the few hundred nanometer decay length (squares) shows a far-field artifact—leading to similar signal increase as the near-field response. *Dashed lines* added as guide for the eye.

molecules with the tip in force feedback at $d = 0$ nm³ vs tip retracted by several 100 nm. When the tip is within several nanometers above the sample surface, a strong increase in Raman intensity is observed for both adsorbates (spectra denoted $SWNT^{tip}$ and MG^{tip}). Note that the difference in noise level from the $SWNT$ to the MG spectra is due to different spectral resolution settings of the spectrometer. Although frequently used to assign the observed TERS signal, a simple comparison of surface vs tip-scattered Raman intensities renders near- and far-field processes a priori indistinguishable. The inset of Fig. 6 shows the Raman peak intensity as a function of the tip–sample distance obtained in two similar experiments for MLs of MG molecules adsorbed on a flat Au surface. The overall increase in signal is comparable in both cases, and an estimate of the Raman enhancement factor gives $G > 10^6$ (*vide infra*). However, with the distance variation occurring on a length scale correlated with pump wavelength or focus dimensions, in one case, the enhancement can solely be attributed to far-field effect (squares). A true near-field effect manifests itself in a correlation of the spatial signal variation with the tip radius (~ 20 nm). Here, with high-quality tip (sharp apex, smooth tip shaft),

³Here, $d = 0$ nm is defined as corresponding to a 20–30% decrease in the shear-force amplitude

the near-field contribution can dominate the overall signal (circles). Therefore, for the tip-scattered Raman signal, only the demonstration of a clear correlation of the lateral or vertical tip-molecule distance dependence with tip radius allows for an unambiguous near-field assignment of the optical response [73]. This is true for all near-field microscopies including *s*-SNOM and the special case of TERS [16, 19, 59, 65].

Experimental Quantification of the Near-Field Raman Enhancement

In contrast to SERS, where the quantification of the enhancement is generally a difficult task, for the tip-scattering experiment, the Raman enhancement factor can be derived from comparison of tip-enhanced vs far-field response of the same surface ML.

Figure 7 shows the spectrally resolved tip-scattered Raman signal during approach of ~ 1 ML of MG on gold (2 nm/step, 1 s/spectrum acquisition time). The pump light is polarized along the tip axis (p^{in}) and the Raman signal is detected unpolarized. Although a faint Raman signature of the molecules is observed with the tip at $d > 100$ nm, a clear molecular fingerprint is obtained only when the tip is within ~ 20 nm from the sample. The prominent bands around 1,615 and 1,365 cm^{-1} are assigned to combinations of the C=C stretching vibrations of the phenyl ring and the mode at 1,170 cm^{-1} is due to a methyl group rocking mode or an in-plane C-H bending mode of the phenyl ring [156].

The enhancement is confined to a tip-sample spacing of just several nanometers and correlated with the apex radius of the tip, as expected for the near-field signature. The increase in Raman response is accompanied by a weak rise in a spectrally broad fluorescence background that has been subtracted. With the molecular fluorescence being quenched due to the electronic

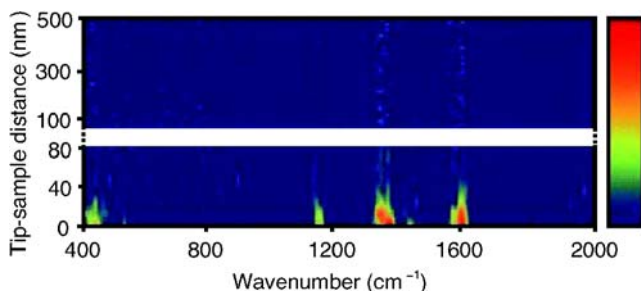


Fig. 7 Tip-sample distance dependence of spectrally resolved Raman signal during approach of ~ 1 ML of MG on gold. Each spectrum is acquired for 1 s and the approach is realized with 2-nm increments. Near-field tip-enhanced signal is observed with the tip within ~ 20 nm above the sample, displaying typical Raman modes for MG molecules [81].

coupling to the metal substrate, this emission could largely be attributed to the enhancement of the intrinsic tip luminescence in conjunction with excitation of plasmonic modes in the tip-sample cavity [152, 157], i.e., its origin is independent of the molecular adsorbates.

With the near-field character of the Raman response verified, the experimental field-enhancement factor can be derived from comparison of the tip-enhanced vs far-field response from the same surface ML. For the experiments presented here, the integrated Raman signal over the 1,150–1,650 cm^{-1} spectral region is used after background subtraction.

As shown in the “[Calculation of the Near-Field Distribution at the Tip-Apex](#)” section, the electromagnetic near-field enhancement originates from a sample surface area approximated by the area of the tip apex. For the evaluation of the enhancement factor, the different areas probed in the near-field (TERS) and far-field (FF) cases are then taken into account. For the TERS setup, the illumination focus has a diameter $d \simeq (\lambda/\text{NA}) \times 1.5 = 2.7 \mu\text{m}$ (the empirical factor of 1.5 accounts for the deviation of the laser beam from a perfect gaussian profile). Considering the $\sim 70^\circ$ angle of incidence of the pump light with respect to the surface-normal in our setup, the actual surface region illuminated is elongated elliptically and larger, with a total area of $\sim 17 \mu\text{m}^2$. In the case of the confocal-Raman setup (FF) used to record the far-field spectrum of MG, the same laser illuminates an area of 870 nm^2 . The molecule is estimated to occupy a surface area of $\sim 0.87 \text{ nm}^2$ (actual 3D space filling: $1.18 \times 1.39 \times 0.98 \text{ nm}$). One ML surface coverage then corresponds to approximately 10^6 molecules in the focus of the far-field setup, and only < 200 are responsible for the tip-enhanced signal for a tip with 10-nm apex radius.

In addition, the detection efficiencies for the two different experimental arrangements are considered. The far-field response is emitted only in half space (solid angle $\Omega = 2\pi$) assuming an isotropic dipolar intensity pattern, and with $\text{NA} = 0.9$, a total of $\sim 27\%$ of the Raman signal is detected, in contrast to the TERS experiments with $\sim 2\%$ for $\text{NA} = 0.35$ and assuming the emission pattern following a $\cos^2(\theta + \frac{\pi}{2})$ dependence ($\theta \in [0, \pi]$).

Taking all these factors into consideration, the Raman enhancement factor can be estimated, and it is found to range from 10^6 to 10^9 , with variation mostly depending on the tip used. This enhancement is expected to be electromagnetic in origin. The molecules experience the tip-enhanced local-field $E_{\text{loc}}(\nu_i) = L(\nu_i) E(\nu_i)$, with $L(\nu_i)$ as the enhancement factor of the incident field $E(\nu_i)$. The concomitant enhancement of the polarization $P(\nu_s)$ at the Raman-shifted frequency

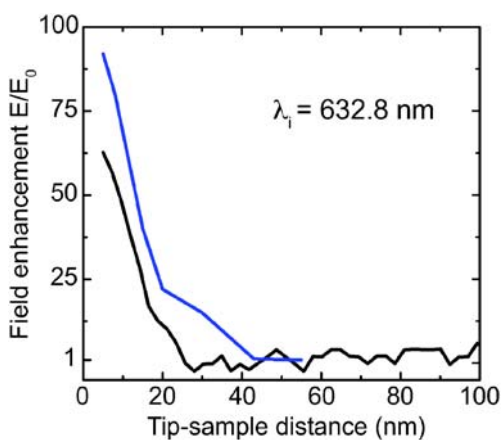


Fig. 8 Field enhancement (E/E_0) for two different Au tips approaching ~ 1 ML of MG on a gold surface. The Raman response is integrated over the dominant peaks in the 1,150–1,650 cm^{-1} spectral region after background subtraction. The enhancement factor is calculated according to $I_{\text{TERS}} \propto E^4$.

v_s is $L'(v_s)$. Therefore, the total field enhancement is given by $L(v_i) \cdot L'(v_s)$ [93, 137]. With the Raman intensity $I \propto |L(v_i) \cdot L'(v_s) \cdot E(v_i)|^2$, the total Raman enhancement factor G is given by $G = |L(v_i) \cdot L'(v_s)|^2$ [158]. Although different in general, the field enhancement factors $L(v_i)$ and $L'(v_s)$ for pump and Raman polarizations, respectively, can be assumed to be similar in this case [159, 160]. This is motivated by both the spectrally broad plasmonic resonance of the tip and its small red-shift upon approaching the sample surface [95, 132, 161].

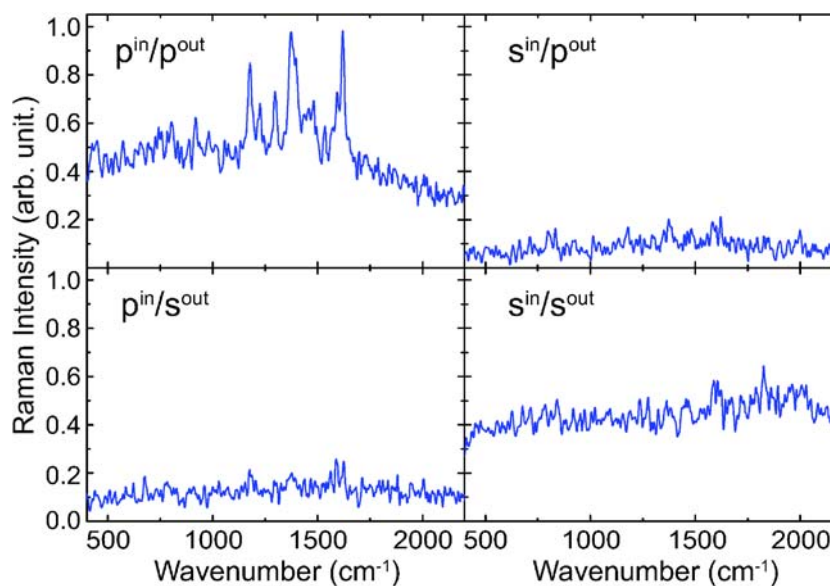
Figure 8 shows the effective field enhancement factors ($L(v_i) \cdot L'(v_s) = E/E_0$) for the integrated Raman

signal from ~ 1 ML of MG on gold as a function of tip-sample distance for two different Au tips (both with $r < 15$ nm). Maximum enhancements of ≥ 90 and ≥ 60 (black and blue curves, respectively) are obtained considering a variation of the tip-scattered Raman response with the fourth power of the electrical field, as indicated above. The molecules adsorbed on the planar Au surface already experience a field enhancement given by the Fresnel factor due to reflection of the incident light at the surface [162]. At 633 nm and $\theta = 70^\circ$, the Fresnel factor is equal to 0.95, resulting in an electric field enhancement of 1.95. We will therefore also derive the total enhancement with respect to the free molecule response.

The study of the polarization dependence of the Raman response offers additional insight into the electromagnetic enhancement of TERS. Figure 9 shows near-field Raman spectra from ~ 1 ML of MG on gold for the different polarization combinations of both pump and Raman light. Incident laser power and acquisition times are identical for all spectra. The polarization directions are defined as parallel (p) and perpendicular (s) with respect to the plane of incidence formed by the incoming wave vector $k(\omega_i)$ and the tip axis. No background has been subtracted and the data are normalized with respect to the intensity of the 1,615 cm^{-1} mode measured in the $p^{\text{in}}/p^{\text{out}}$ polarization configuration (upper left panel).

With the incident field polarized perpendicular to the tip axis (s^{in}), almost no Raman signal is observed, irrespective of the polarization of the scattered light. In contrast, with the pump polarized along the tip axis (p^{in}), clear Raman fingerprints of MG molecules

Fig. 9 Polarization dependence of the near-field tip-enhanced Raman response originating from ~ 1 ML of MG on gold. All spectra are acquired for 30 s and normalized to the maximum intensity value of the 1,615- cm^{-1} mode in $p^{\text{in}}/(\text{unpol.})^{\text{out}}$ geometry. A very weak Raman response is observed for polarization combinations other than $p^{\text{in}}/p^{\text{out}}$, where strong near-field coupling gives rise to a strong Raman enhancement. The spectrally broad background is due to the intrinsic luminescence from the Au tip itself.



are observed, with the Raman response being predominantly polarized parallel to the tip ($p^{\text{in}}/p^{\text{out}}$) as expected for near-field TERS from isotropically distributed molecules with diagonal Raman tensor components as is the case of MG. For both the $s^{\text{in}}/p^{\text{out}}$ and the $p^{\text{in}}/s^{\text{out}}$ configuration, only a weak specific vibrational Raman signal is observed due to the absence of the tip-sample optical coupling. For $s^{\text{in}}/s^{\text{out}}$, a larger background is observed, albeit with no Raman enhancement, as expected.

The highly polarized TERS response observed in our experiments indicates the absence of significant near-field depolarization for the homogeneous and slender tip geometries used. This is required for symmetry-selective probing in TERS and other non-linear tip-enhanced processes [163–165] (Neacsu et al., unpublished manuscript) that rely on polarization selective and conserving light scattering. In contrast, for a Ag-particle-topped quartz AFM probe as used for probing the 520-cm^{-1} Raman band of Si [166], the observed Raman depolarization has been attributed to the wide cone angle of the tip [119].

TERS of Molecular Adsorbates

In Fig. 10, representative tip-enhanced Raman spectra are shown for MG on smooth Au surfaces. They are acquired for the same surface coverage of ~ 1 ML, but using different tips exhibiting enhancements of 3×10^8 (a), 7×10^7 (b), 1×10^7 (c), and 1×10^6 (d), respectively. The experimental uncertainty is estimated at a factor of 3–5 for each value. The tip-enhanced Raman spectra are reproducible for a given tip. However, as seen from the data, the spectral details vary from tip to tip with increasing enhancement. With the lateral confinement of the tip-enhancement within a ~ 10 -nm-diameter surface region and a molecular density of $\sim 1/\text{nm}^2$, we estimate that the signal observed in Fig. 10a–d originates from ~ 100 molecules.

In the lower panel of the figure, the far-field Raman spectrum from the same sample is shown for comparison (black line). The far-field spectrum closely resembles that in aqueous solution [156], indicating that the molecules are physisorbed in isotropic orientation at the surface. The blue bars represent normal Raman modes of the MG anion calculated using density functional theory as implemented in Gaussian03 as discussed in [81]. The assignment and spectral position of the calculated modes agree well with literature values [156, 167].

For moderate near-field enhancements $\leq 10^7$, both spectral positions and relative intensities of the modes

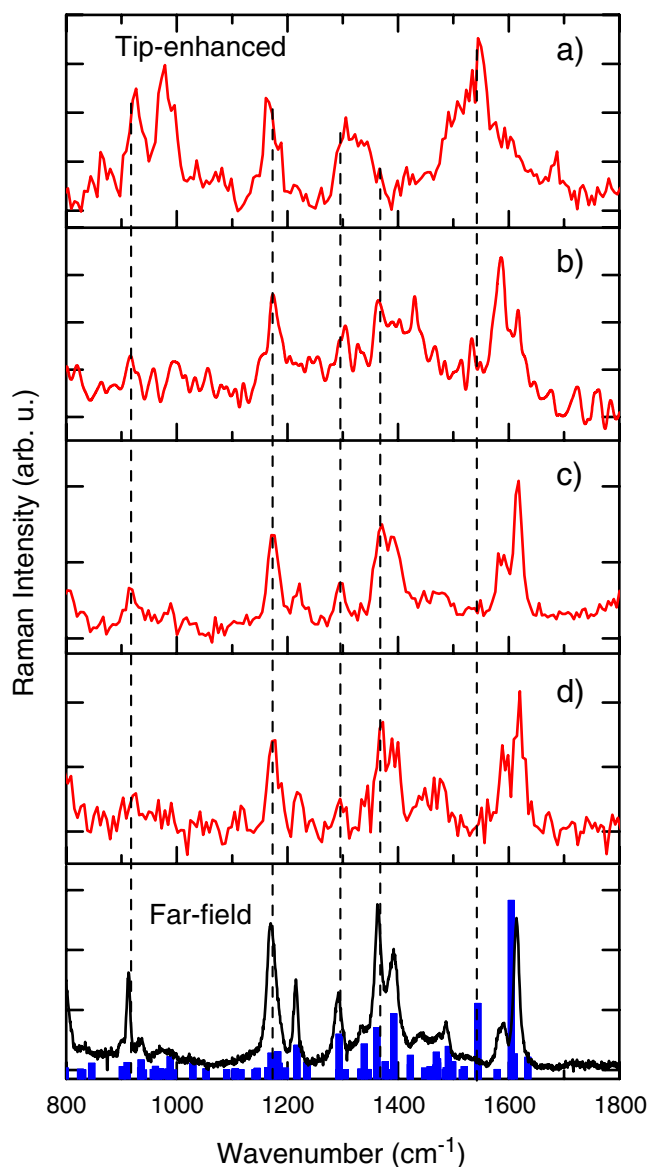


Fig. 10 Tip-enhanced Raman spectra for ~ 1 ML of MG for different degrees of enhancement (a, b, c, d) in comparison with the corresponding far-field Raman spectrum (bottom graph) and DFT calculation for the mode assignment (blue bars). The Raman enhancement factors derived are 3×10^8 (a), 7×10^7 (b), 1×10^7 (c), and 1×10^6 (d), respectively. Data are acquired for 1 s (a), 100 s (b, c), and 30 s (d), respectively. Spectral resolution is 25 cm^{-1} for the near-field and 1 cm^{-1} for the far-field spectra [96].

resemble the far-field signature, as seen in Fig. 10c and d and in accordance with other TERS results for similar enhancements [79]. However, with increasing enhancement of 7×10^7 (b), and most pronounced for 3×10^8 (a), the vibrational modes start to look markedly different. While some of the modes are present in both far-field and near-field spectra (e.g., those at: 920 , 1170 , and 1305 cm^{-1}), some others are only present in the highly enhanced near-field results (e.g., 1365 ,

1,544 cm^{-1}). The vertical dashed lines in Fig. 10 are added as a guide to the eye for easier comparison.

The DFT calculation allows for the identification of the spectral features in the far-field data of Fig. 10. The majority of the intense Raman modes can be attributed to modes either localized at the phenyl ring or delocalized over the two dimethylamino phenyl groups. In the spectral region of 910 to 980 cm^{-1} , several vibrational modes, typically characterized by in-plane skeletal bending and/or out-of-plane C-H motions, are found. The 1,170- cm^{-1} mode may be assigned to a methyl group rocking mode or an in-plane C-H bending mode of the phenyl ring. Around 1,300 cm^{-1} , in-plane C-H deformation modes and C-C stretching modes of the methane group are located.

Furthermore, the calculations show that the new spectral features seen in the highly enhanced near-field spectra in Fig. 10 mostly correspond to vibrational normal modes of MG. Among the characteristic near-field enhanced modes, e.g., the peak at 1,365 cm^{-1} , which is very strong in the far-field spectrum but decreases with increasing enhancement, can be assigned to combination of the C=C stretching motions of the aromatic ring. In contrast, the prominent peak at 1,544 cm^{-1} , which dominates for the highest enhancement is very weak for small enhancements or in the far-field spectra. Here, the calculation shows a mode characterized by stretching motions combined with in-plane C-H bending motions of the conjugated di-methyl-amino-phenyl rings. The two modes at 1,585 and 1,615 cm^{-1} , which can be assigned to C=C stretching vibrations of the phenyl ring, decrease with enhancement.

This change in both intensity and spectral signature with increasing near-field enhancement together with the vibrational analysis shows that the Raman peaks observed correspond to vibrational modes of MG, whereby different selection rules seem to apply for the Raman spectra obtained under condition of high enhancements [158].

In the following, we discuss different physical mechanisms possibly responsible for this mode selectivity. Due to the high localization of the optical near-field, the molecules in the tip-sample gap experience a large field gradient and different Raman symmetry selection rules can come into play [168–170]. The relevant terms of the dipole moment μ_a of a molecule situated in the presence of a high field-gradient are:

$$\mu_a = \left\{ \left(\frac{d\alpha_{ab}}{dQ} \right)_0 E + \left(\frac{d\mu_a^p}{dQ} \right)_0 E + \alpha_{ab} \left(\frac{dE}{dQ} \right)_0 + \frac{1}{3} \frac{\partial E}{\partial c} \left(\frac{dA_{abc}}{dQ} \right)_0 \right\} Q,$$

with E as the amplitude of the applied electric field, μ_a^p the permanent molecular dipole moment, α_{ab} the polarizability tensor at vibrational frequency, and A_{abc} the quadrupole polarizability [171]. Q represents the coordinate of vibration and $\{a, b, c\}$ are a permutation of the coordinates $\{x, y, z\}$.

The first and second terms of the equation describe the normal Raman emission and the IR absorption, respectively. For an IR mode to be active, a variation in the dipole moment along the vibration coordinate is necessary [172]. The presence of the field gradient fulfills this requirement and thus allows for IR modes to become Raman active in that case. However, for MG, it was found that the few IR modes show no significant resemblance with the highly enhanced TER spectra (details in [81]).

The third term denotes the gradient field Raman (GFR) effect [171]. The mechanism by which strong field gradients can influence the molecular Raman spectra by altering the selection rules require that the polarizability tensor (α_{ab}) and $(dE_b/dQ)_0$ must simultaneously be nonzero. The resulting selection rules resemble the surface selection rules [173] and give rise to GFR lines observed in addition to the normal Raman modes.

The optical field gradient can also couple to vibrations via the derivative of the quadrupole polarizability A_{ijk} of a mode, as described by the last term of the above equation [170]. With α_{ab} and A_{ijk} transforming differently in terms of symmetry and their ratio being highly mode-dependent, this could also account for the mode selectivity observed in tip-enhanced Raman scattering [174]. This might help to resolve the striking observation that the strength of the calculated four modes at 846, 988, 1,029, and 1,544 cm^{-1} are overestimated by DFT calculation as compared to the far-field spectra, but coincidentally represent modes that are relatively strongly enhanced in the TER spectra.

While it is difficult to quantify the contribution of GFR in general [171], the occurrence of normally forbidden modes in the TERS results suggest that the process contributes in this case. Similar differences between far- and near-field Raman spectra were reported previously in fiber-based SNOM experiments on Rb-doped KTiOPO_4 [20, 21].

In addition, the resonant Raman excitation leads to a coupling of electronic with vibrational transitions, resulting in different selection rules. Such vibronically allowed transitions may further be influenced by the presence of the strong field gradient and will affect the relative peak amplitude of the observed Raman modes [172]. This effect would resemble the “chemical effect” observed in SERS [35].

The pronounced spectral differences between the tip-enhanced and far-field Raman response have similarities to observations made in SERS, where vibrational modes that are normally not Raman allowed had been found [175–177]. Aside from orientational effects, these spectral variations are typically interpreted to arise from conformational changes and/or transient covalent binding of the molecule at “active sites” [173]. With that being unlikely in the tip-enhanced Raman geometry discussed here, this indicates that the kind of spectral selectivity observed in our TERS experiments should be attributed primarily to electromagnetic mechanisms.

Molecular Bleaching

An important question regarding the appearance of different spectral features in the near-field tip-enhanced Raman spectra is the influence of the molecular bleaching or other decomposition products [178, 179].

With the molecules under investigation exposed to the strongly localized and enhanced near-field, this leads to a sometimes rapid photo-decomposition process, especially in a resonant Raman excitation.

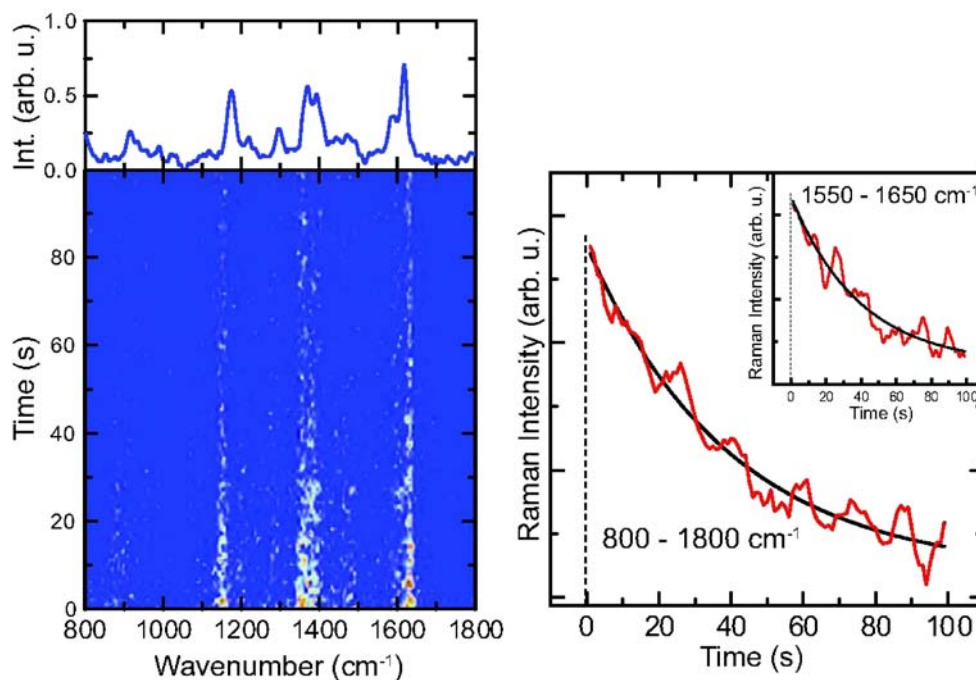
To probe for the possible appearance of photoreaction products and their signature in the Raman spectra, the evolution of the Raman emission is monitored in time-series experiments. Figure 11 (left panel) shows consecutive near-field Raman spectra acquired for 1 s

each for an enhancement of 1.3×10^7 with an incident laser fluence of 3×10^4 W/cm². The molecules bleach on a time scale of ~ 100 s, depending on the enhancement level, and the decay and subsequent disappearance of the spectral response is uniform, i.e., the relative peak amplitudes are maintained. During the bleaching, no new spectral features appear from possible photoreaction products and the signal decays with the relative peak amplitudes remaining constant. After complete bleaching, no discernible Raman response can be observed. The fluctuation observed in the time series is expected given the small number of ~ 100 molecules probed in the near-field enhanced region under the tip apex. The sum over all spectra (top graph) or the sum of any large enough subset even at later times, i.e., after substantial bleaching has already occurred, closely resembles the far-field response of MG and, thus, allows us to attribute the Raman response to MG molecules.

The same behavior of a gradual and homogeneous disappearance of the Raman response without a relative change in peak intensity is also observed for larger enhancements, i.e., the case where a different mode structure is observed. However, the larger local field experienced by the molecules leads, in general, to decreasing decay time constants.

Figure 11 (right panel) shows the decay kinetics of the spectrally integrated Raman intensity for the time series data shown on the left. This is shown in comparison to the integral intensity of the region from

Fig. 11 *Left:* Time series of 100 consecutive near-field Raman spectra (acquired for 1 s each) for ~ 1 ML MG on Au (Raman enhancement 1.3×10^7). The signal decays to zero due to bleaching and no new spectral features appear from the photoreaction products. The sum Raman spectrum (*top panel*) clearly resembles the far-field spectrum. *Right:* Bleaching kinetics derived for the spectrally integrated Raman time series and the region from 1,550 to 1,650 cm⁻¹ (*inset*) [96].



1,550 to 1,650 cm^{-1} encompassing only the two prominent modes (inset). Assuming an exponential decay behavior of $I/I_0 = \exp(-t/\tau)$ for the Raman intensity, a decay time $\tau = 40 \pm 5$ s is derived for both cases (solid lines). From the applied laser fluence of 3×10^4 W/cm^2 and the enhancement of the pump intensity of $\sim \sqrt{1.3 \times 10^7}$, the bleaching is induced by a local pump fluence of 4.7×10^7 W/cm^2 .

An extreme case of molecular bleaching is shown in Fig. 12. A time series of 100 consecutive Raman spectra from a sample with submonolayer molecular coverage, with each spectrum acquired for 1 s, is recorded. The estimated Raman enhancement factor is 9×10^7 , and the spectral features deviate from the far-field Raman spectrum presented in Fig. 10b, akin to the spectra shown in panels a and b of the same figure for high enhancement level (e.g., the mode at 1,544 cm^{-1}). After an illumination time of about 50 s, the overall Raman intensity drops suddenly over the whole spectral region, and most visible for the peak at 1,306 cm^{-1} , but no new spectral features emerge. Thus, even for extreme cases

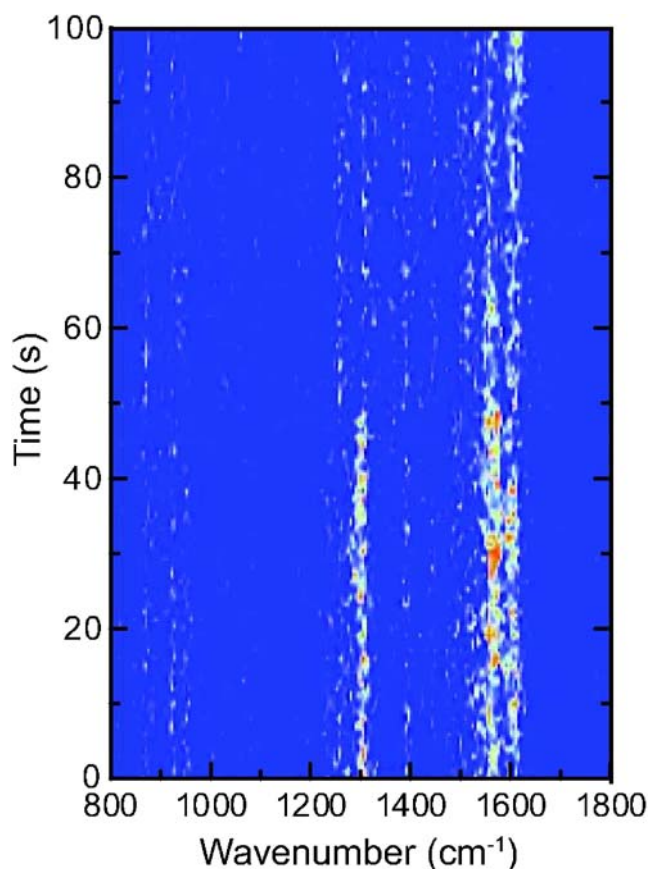


Fig. 12 Time series of 100 near-field Raman spectra acquired for 1 s each. After ~ 50 s, the Raman intensity reduces due to bleaching, but no signature of secondary products is visible.

of bleaching, the molecular decomposition products do not contribute to the observed Raman signal.

It was suggested that the molecular bleaching rate could be used for the derivation of the enhancement factor [112]. It should be noted that the bleaching rate is not a characteristic physical quantity universal for a given molecule. For example, MG isothiocyanate—a sister dye of MG—was found to bleach with a rate constant more than two orders of magnitude higher than the MG studied here [112], if renormalized to the same experimental conditions. Bleaching mechanisms can be quite diverse [180]. They may include irreversible photoinduced or even multiphoton induced reactions such as rearrangements, dissociation and fragmentation, elimination or hydrogen abstraction, or perhaps photooxidation with ambient oxygen via triplet states. It can depend on, e.g., humidity or cleanliness of the tip or sample, and is, hence, not a useful measure to compare experiments performed under different conditions in different laboratories.

With the experiments carried out under ambient conditions, special care must be taken to use clean samples and tips. It is well known [181] that contaminating organic compounds and/or carbon residues can adhere to either tip or sample and reveal their Raman signature in the tip-enhanced spectra, e.g., Raman bands of appreciable intensity at frequencies above 1,750 cm^{-1} for carbon [182].

A carbon cluster Raman response (see Fig. 6 in [96]) manifests itself in characteristic spectral features much different from the spectral response discussed above for ML or submonolayer MG. In accordance with previous observations [181–183], the carbon Raman response is comparatively large and fluctuates rapidly in an uncorrelated way. In contrast to the data on MG, a distinct spectral feature emerges around 2,000 cm^{-1} , which has been assigned to, e.g., modes within the segments of carbon chains [182], and which is absent in the TERS spectra of MG. This absence of the carbon Raman response can be understood since the bleaching of ML and submonolayer MG coverage leads to smaller molecular fragments and, subsequently, to a dilute surface carbon distribution and, hence, does not lead to extended carbon chains and aggregates, which can readily form by multilayer MG decomposition at ambient temperatures.

Besides the degradation of the analyte, another potential source of carbon contamination is the near-field probe itself. At room temperature and in a noncontrolled atmosphere, contaminants from the environment could adsorb onto the tip surface and reveal highly enhanced Raman signals. TERS control experiments with the bare tip and clean Au samples

prior to MG deposition were carried out to confirm the absence of vibrational Raman signature. Only intrinsic tip luminescence has been observed in that case [81].

TERS with Single Molecule Sensitivity

With the measured tip-enhanced Raman spectra presenting a signal-to-noise ratio of more than 40:1 when probing ~ 100 molecules for 1 s accumulation time, this demonstrates the potential for even single-molecule sensitivity. Figure 13 shows near-field tip-enhanced Raman spectra measured in a time series with 1 s acquisition time for each spectrum for a sample prepared with submonolayer surface coverage, adjusted to expect on average < 1 molecule under the tip-confined area of $\sim 100 \text{ nm}^2$.

Here, the tip has been held at a constant distance of $d = 0 \text{ nm}$ above the sample and the total Raman enhancement was estimated at 5×10^9 .⁴ The observed Raman signal exhibits temporal variations of relative peak amplitudes and fluctuations in spectral position. These are characteristic signatures of probing a single emitter in terms of an individual molecule. Similar observations have been made before in SERS [37–39, 41] with the fluctuations in the spectroscopic signature of a single emitter typically attributed to changes in its local environment, its structure, molecular diffusion [36, 184], and changes in molecular orientation [179]. With MG only physisorbed, it has to be considered in particular that the molecules can diffuse in and out of the apex-confined probe region while experiencing different degrees of enhancement. The diffusion dynamics can be facilitated by the thin water layer present on the sample surface under ambient conditions.

In the time series in Fig. 13, the apparent bleaching rate seems reduced compared to what is expected from the analysis of the ensemble bleaching discussed above. This is a result of the dilute surface coverage where new molecules directly neighboring the tip–sample gap diffuse into the near-field enhanced region. However, the signal vanishes rapidly after 100 s due to the depletion of molecules in the immediate near-apex region.

A different mode structure of single-molecule MG Raman is observed compared to the far-field response—especially pronounced for the $1,500\text{--}1,600\text{-cm}^{-1}$ spectral region, akin to the results for the ensembles under strong enhancements shown above. Figure 13 (middle panel) displays the sum spectrum

(olive) for the single-molecule response time series (left) in comparison with ensemble spectra of ~ 100 molecules probed for 1 s (red) showing different degrees of enhancement: 3×10^8 in a and 7×10^7 in b. Panel c presents the sum spectrum (blue) of the data shown in Fig. 11a that, as for a moderate enhancement, closely resembles the far-field spectrum. The resemblance of the Raman spectrum of a molecular ensemble with the sum spectrum over the whole time series offers strong evidence of probing single intact MG molecules [40]. Note that the sum over the times series shall therefore resemble an ensemble spectrum for large enhancement rather than the far-field Raman spectrum. In assessing the resemblance of the spectral characteristics, it has to be considered that, at low coverage, the molecules have more degrees of freedom to dynamically change orientation and they can diffuse. Given the rather weak response, the signal detected can only be expected to emerge from the region of largest enhancement, and with the diffusing molecules probing the spatial variation of the enhancement under the tip, this corresponds to an extreme case of inhomogeneous broadening. Therefore, while individual spectral features at positions in accordance with the strongly tip-enhanced near-field response are observed in the time series, the sum spectrum no longer exhibits clearly resolved lines. This interpretation is further corroborated considering, e.g., the improved resemblance of the peak in the $1,550\text{--}1,600\text{-cm}^{-1}$ region of the single molecule sum spectrum with the sum of the two near-field spectra (in a and b) of different enhancement.

Further insight is obtained by studying the statistical behavior of the single-molecule Raman response [36]. Figure 13 (right panel top graph) displays the integrated $1,430$ to $1,650 \text{ cm}^{-1}$ spectral intensity for the data in the left panel. The signal intensities cluster with intervals of $170\text{--}230 \text{ counts}\cdot\text{s}^{-1}$, as already evident from visually inspecting the time-series of integrated intensities (dashed lines), and this manifests itself in the corresponding histogram in an asymmetric distribution with discrete peaks (inset). This behavior is qualitatively reproducible for experiments with the same surface coverage, and it can be interpreted as the Raman emission from $n = 0$ (noise peak), 1, 2, and 3 molecules being probed under the tip, as suggested for similar findings in SERS [34, 36]. This assignment is corroborated from experiments with different surface coverages: for lower coverages, only the $n = 0$ and 1 peaks remain, and with increasing coverage, the distribution converges to a narrow random Gaussian distribution, which is observed from a large molecular ensemble, as seen in the lower panel, where 100 consecutive far-field spectra were acquired for 100 s each and the signal is

⁴Here, $d = 0 \text{ nm}$ is defined as corresponding to a 20–30% decrease in the shear-force amplitude.

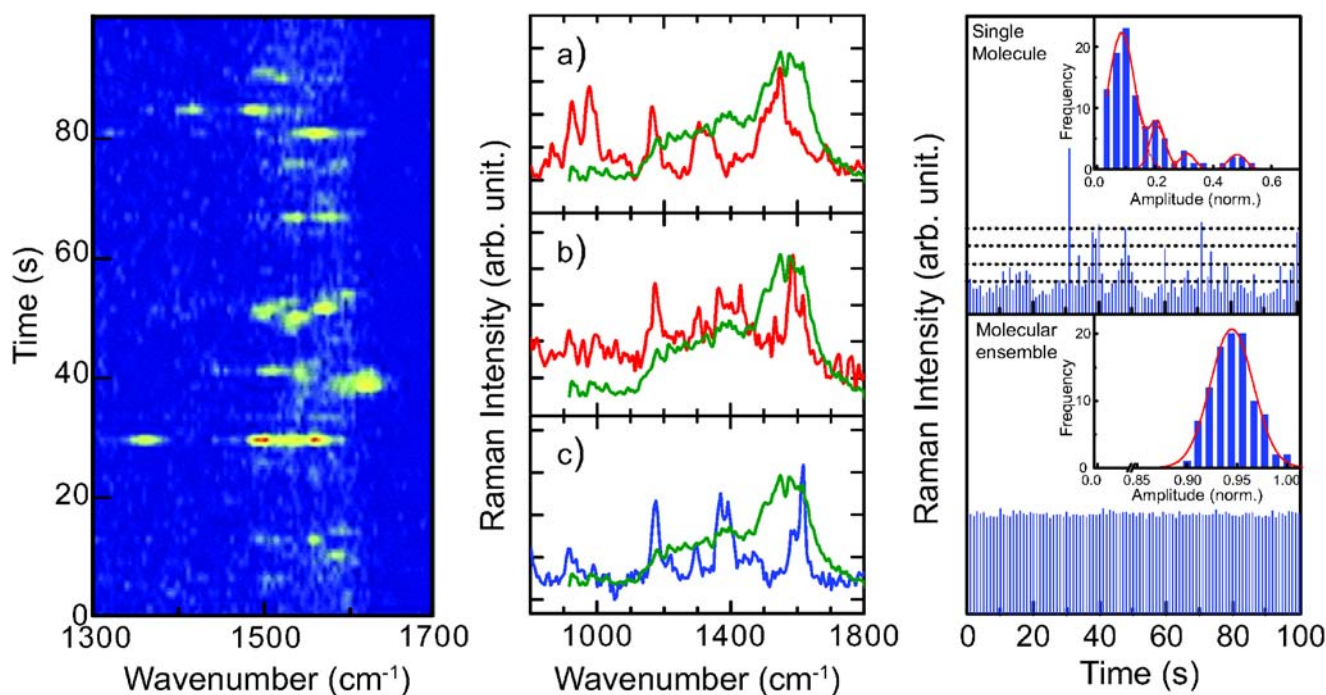


Fig. 13 *Left:* Time series of tip-scattered Raman spectra for a submonolayer MG surface coverage with Raman enhancement of 5×10^9 . The spectral diffusion observed is characteristic for observing single MG molecules. *Middle:* Comparison between sum spectrum of data shown in left panel (*olive*) and tip-enhanced Raman spectra for different degrees of enhancement (*red*, *a* and *b*) and sum spectrum of data shown in Fig. 11 (*blue*). *Right:* Temporal variation of the Raman intensity of the inte-

grated 1,480–1,630 cm^{-1} of time series shown in left panel (*top*). From the corresponding histogram (*inset*) a discretization of Raman intensities can be seen with 170–230 counts·molecule $^{-1}$ ·s $^{-1}$ (dashed line increment). For comparison, temporal variation of the Raman intensity of the integrated 1,480–1,630 cm^{-1} of big molecular ensemble (far-field) is shown (*bottom*) together with the corresponding histogram (*inset*) [81, 96].

integrated over the same spectral range as in the case of the single-molecule experiment. The details of the histogram, however, depend on the binning procedure, especially for a small data set, as has been shown to be insufficient as the sole argument for single-molecule observation [185].

The optical trapping and alignment of MG under the tip must also be considered as a possible source of the observed surface diffusion and intensity fluctuations [186]. However, for MG together with our particular experimental conditions, this cannot explain the discretization of Raman peak intensities in the single-molecule response, as detailed elsewhere [81].

Our single-molecule TER results are similar to other recent experimental findings [85] where brilliant cresyl blue (BCB) molecules adsorbed on planar Au were probed. For enhancements of $\sim 10^7$ similar to our intermediate values, temporal fluctuations in both intensity and mode frequency were observed, albeit with no significant spectral differences between the far-field and near-field response, as seen here for high enhancements. Recently, spatially resolved TERS imaging and identification of individual BCB molecules directly con-

firmed our single-molecule assignment in the Raman response in the results discussed above [187].

Raman Imaging of Nanocrystals: Near-Field Crystallographic Symmetry

With the TERS capability of detecting molecules down to the single emitter level, it is highly desirable to extend the technique to also probe other classes of materials such as crystalline nanostructures. While far-field Raman microscopy has been successfully used for such investigations [188, 189], the applicability of TERS has not yet been explored.

In the following, we propose and discuss the potential of TERS for the spatially resolved determination of the crystallographic orientation of crystalline materials by taking advantage of the fundamental interaction of the Raman process with lattice phonons together with the symmetry properties and selection rules of the tip-enhanced scattering. While the application of the symmetry properties of the Raman selection rules in a tip-enhanced geometry has been emphasized

previously [119, 190–192], no discussion of the applicability to crystalline nanostructures has yet been provided.

With Raman scattering being less invasive than electron or X-ray techniques and applicable in situ, this approach will fill a much needed gap in the characterization of nanostructured materials with increasing complexity [193, 194]. Transmission electron microscopy, capable of providing atomic resolution [195], requires samples thin enough to be transparent for electrons, extensive sample preparation, and vacuum conditions, making in situ experiments difficult [196]. Likewise, X-ray microscopy is capable of characterizing nanostructures with atomic resolution [197], but it requires a monochromatic brilliant synchrotron radiation source and radiation beam damage remains a concern [198]. Here, the comparable simplicity of TERS from an instrumentation perspective makes it highly attractive, providing complementary information and even avoiding some of the disadvantages of the existing techniques.

In Raman spectroscopy, the specific phonon modes probed depend on the chosen experimental geometry, in terms of the incident and detected polarization, as well as the propagation direction of light [5, 199]. These phonon modes allow determination of the crystallographic orientation of a sample. This has been shown in far-field Raman in, e.g., the study of 90° domain switching in bulk BaTiO₃ [200] or the observation of ferroelastic domains in LaNiO₄ [201]. However, in Raman microscopy, in the commonly used confocal epi-illumination and detection geometry, this reduces the available degrees of freedom, thus resulting in the loss of the general capability to probe the symmetry-specific Raman tensor elements. In extending the use of the Raman selection rules to a side-illuminated TERS geometry, these degrees of freedom can be regained and even further refined by taking into account the tip geometry.

The intensity of the Raman scattered light from a medium is given by: $I_s \propto |\vec{e}_s \cdot \vec{R} \cdot \vec{e}_i|^2$, where \vec{e}_i and \vec{e}_s are the polarization of the incident and scattered light, respectively, and the Raman tensor \vec{R} is the derivative of the susceptibility tensor [202]. As an example, for a Raman-active phonon mode of tetragonal BaTiO₃, \vec{R} is given by:

$$\mathbf{A}_1(\vec{\xi}) = \begin{pmatrix} a & 0 & 0 \\ 0 & a & 0 \\ 0 & 0 & b \end{pmatrix},$$

where $\vec{\xi}$ denotes the polarization direction of the mode (for polar modes). The symmetry of a given mode, in

this case A_1 , is determined from group theory and may contain multiple component phonon modes of different frequency [203]. Thus, when the polarization conditions, determined from the susceptibility derivative, are satisfied for a given symmetry mode, the Raman shift due to the phonons belonging to that mode can be observed.

In addition, one can selectively isolate specific phonon modes within a symmetry mode. For polar modes, the phonons will separate into transverse optical (TO) and longitudinal optical (LO) components [204], which, being distinct in frequency, can be spectrally resolved. The Raman tensor methods described above do not account for the distinct frequencies of TO and LO modes nor describe how to selectively excite these, requiring further refinement of the selection rules

For a given geometry, the wavevector \vec{q} of the propagating phonon can be determined by conservation of momentum from the wavevectors of the incident and scattered light. Based on the relative orientation between \vec{q} and $\vec{\xi}$, one can selectively excite the LO mode for $\vec{q} \parallel \vec{\xi}$, or the TO mode for $\vec{q} \perp \vec{\xi}$. Thus, the observation of either a TO or an LO mode provides the additional information about the orientation of the crystallographic axes.

Furthermore, drawing on the nanoscopic apex of a plasmonic tip for preferential enhancement of incident light polarized along the tip axis allows us to exploit the unique symmetry selection rules associated with the tip [92], selecting modes with polarizations parallel to the tip axis. Modes for which either the incident or scattered polarization coincide with the enhancement axis may also be observed, albeit with a lower intensity.

By appropriate selection of the polarization and propagation directions of the incident and scattered light, specific Raman-active phonon modes may be isolated and detected. From the Raman tensor, one can obtain the angular dependence of the Raman scattering intensity for each specific combination of incident and scattered polarizations. A comparison of the corresponding experimental and theoretical emission intensities will allow one to deduce the orientation of the crystallographic axes. Thus, in combination with an *a priori* knowledge of the space group of the crystal and the Raman modes of the material, one can determine the crystallographic orientation of a nanostructure (Berweger et al., unpublished manuscript).

Although the study of nanocrystalline samples opens up a wide range of potential applications for TERS, some fundamental aspects are not yet fully understood. Recent far-field studies of wurtzite CdS nanorods indicate a possible depolarization effect in dielectric

nanostructures, leading to a breaking of the Raman tensor selection rules [189]. Furthermore, it has been shown that the presence of a sharp edge within the near-field of a photoemitter can affect the polarization of the emitted light [205], although the resulting effect on Raman scattering is yet unclear. In addition, the large field gradient near the tip can fundamentally alter the selection rules, making previously silent modes visible [171]. Although this may render IR and other modes Raman-active [206], making mode assignment more difficult, it would still shed further insight into the fundamental material properties.

Outlook

TERS may emerge as an important analytical tool for chemical and structural identification on the nanoscale. It offers chemical specificity, nanometer spatial resolution, single-molecule sensitivity, and symmetry selectivity. However, with both sensitivity and spatial resolution critically dependent on the well defined geometry and related optical properties of the tip, reproducibility has remained an issue in TERS.

Reproducibility can be enhanced performing TERS under controlled experimental environmental conditions. Performing experiments under, e.g., ultrahigh vacuum (UHV) conditions offers variable sample temperature and combination with other UHV techniques for surface analysis [82, 153, 187]. Furthermore, for direct far-field illumination conditions, it is difficult to a priori distinguish the near-field response from the unspecific far-field imaging artifacts (*vide supra*).

Future developments in tip design and fabrication may prove critical. We have recently demonstrated a novel way to generate a nanoconfined light emitter on a nanoscopic probe tip obtained by grating-coupling of SPPs on the tip-shaft [207]. The adiabatic field concentration of the propagating SPP, determined by the boundary conditions imposed by the tapered shape of the tip, offers an intrinsic nanofocusing effect and, thus, gives rise to confined light emission only from the apex region, as theoretically predicted [208].

In this experiment, linear gratings are written onto the shaft of Au tips by focused ion beam milling, $\sim 10 \mu\text{m}$ away from the apex, as schematically shown in Fig. 14a. Upon grating illumination with a broadband light source (150 nm spectral bandwidth of Ti-sapphire oscillator), SPPs are excited and launched towards the apex [155, 209], where they are reradiated, as shown in Fig. 14b (details discussed in [207]).

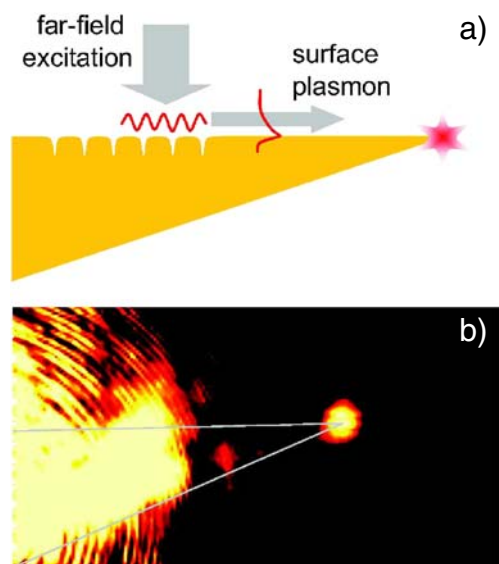


Fig. 14 **a** Principle of the nonlocal excitation of the tip apex. Far-field radiation excites SPP on the grating, which propagate along the shaft towards the tip apex, where they are reradiated into the far-field. **b** Microscope image recorded for illumination of the tip-grid demonstrating the efficient nonlocal excitation of the tip apex via illumination of the grating [207].

Spatially separating the excitation from the apex itself, this approach is particularly promising as it avoids the otherwise omnipresent far-field background present for direct apex illumination. In addition, it would provide the spatial resolution needed for near-field optical techniques including *s*-SNOM and TERS.

Summary

A systematic understanding both experimentally and theoretically of the fundamental processes responsible for field enhancement, spectral tip plasmonic response, and tip-sample coupling has allowed for reaching Raman enhancement factors as high as 10^9 leading to single-molecule sensitivity. With lateral resolution determined by the interplay of the tip apex radius, the tip-sample distance and the dielectric properties of tip and sample materials, nanometer spatial resolution can be obtained. Criteria have been discussed for experimental TERS implementation and distinction of the near-field signature from far-field imaging artifacts. The combination of the inherent sensitivity and spatial resolution of TERS with the Raman selection rules and the unique symmetry of the scanning tip makes possible the spatially resolved vibrational mapping on the nanoscale. Its implementation for

determining the orientation and domains in crystallographic nanostructures has been proposed. Future developments in tip design and more efficient illumination and detection geometries and scanning probe implementation will allow for TERS to become a powerful nano-spectroscopic analysis tool.

Acknowledgements The authors would like to thank Nicolas Behr, Jens Dreyer, Thomas Elsaesser, Christoph Lienau, and Claus Ropers for valuable discussions and support. Funding by the *Deutsche Forschungsgemeinschaft* through SFB 658 (“Elementary Processes in Molecular Switches at Surface”) the National Science Foundation (NSF CAREER grant CHE 0748226 and IGERT Fellowship) is greatly acknowledged.

References

- Chalmers J, Griffiths P, editors. Handbook of vibrational spectroscopy. Chichester: Wiley; 2002.
- Kuzmany H. Solid-state spectroscopy. New York: Springer; 1998.
- Wilson EB, Decius JC, Cross PC. Molecular vibrations: the theory of infrared and Raman vibrational spectra. New York: Dover; 1980.
- Hendra PJ, Stratton PM. Laser-Raman spectroscopy. Chem Rev. 1968;69:325.
- Hendra PJ, Vear CJ. Laser Raman spectroscopy: a review. The Analyst. 1970;95:321.
- Yu PP, Cardona M. Fundamentals of semiconductors. 3rd ed. New York: Springer; 2005.
- Aroca R. Surface-enhanced vibrational spectroscopy. New York: Wiley; 2006.
- Demtröder W. Laser spectroscopy: basic concepts and instrumentation. 2nd ed. New York: Springer; 1996.
- Tabaksblat R, Meier RJ, Kip BJ. Confocal Raman microspectroscopy: theory and application to thin polymer samples. Appl Spectr. 1992;46:60.
- Abbe E. Beiträge zur Theorie des Mikroskops und der mikroskopischen Wahrnehmung. Archiv f Mikroskop Anat. 1873;9:413.
- Strutt (Lord Rayleigh) J. On the theory of optical images, with special reference to the microscope. Phil Mag. 1896;42:167.
- Lewis A, Isaacson M, Muray A, Harootunian A: Scanning optical spectral microscopy with 500 Å resolution. Biophys J. 1983;41:405a.
- Pohl DW, Denk W, Lanz M. Optical stethoscopy: image recording with resolution $\lambda/20$. Appl Phys Lett. 1984;44:651.
- Lewis A, Isaacson M, Harootunian A, Muray A. Development of a 500 Å spatial resolution light microscope. Light is efficiently transmitted through $\lambda/16$ diameter apertures. Ultramicroscopy 1984;13:227.
- Fillard J. Near field optics and nanoscopy. Singapore: world Scientific; 1997.
- Courjon D. Near-field microscopy and near-field optics. London: Imperial College Press; 2003.
- Kawata S, Ohtus M, Irie M. Nanooptics. New York: Springer; 2002.
- Novotny L, Stranick SJ. Near-field optical microscopy and spectroscopy with pointed probes. Annu Rev Phys Chem. 2006;57:303.
- Novotny L, Hecht B. Principles of nano-optics. Cambridge: Cambridge University Press; 2006.
- Jahncke CL, Paesler MA, Hallen HD. Raman imaging with near-field scanning optical microscopy. Appl Phys Lett. 1995;67:2483.
- Jahncke CL, Hallen HD, Paesler MA. Nano-Raman spectroscopy and imaging with a near-field scanning optical microscopes. J Raman Spectrosc. 1996;27:579.
- Webster S, Batchelder DN, Smith DA. Submicron resolution measurement of stress in silicon by near-field Raman spectroscopy. Appl Phys Lett. 1998;72:1478.
- Serio MD, Mohapatra H, Zenobi R, Deckert V. Investigation of the liquid-liquid interface with high spatial resolution using near-field Raman spectroscopy. Chem Phys Lett. 2006;417:425.
- Fleischmann M, Hendra P, McQuillan A. Raman-spectra of pyridine adsorbed at a silver interface. Chem Phys Lett. 1974;26:163.
- Jeanmaire D, Van Duyne R. Surface Raman spectroelectrochemistry. Part I. Heterocyclic, aromatic, and aliphatic amines adsorbed on the anodized silver electrode. J Electroanal Chem. 1977;84:1.
- Albrecht M, Creighton J. Anomalously intense Raman spectra of pyridine at a silver electrode. J Am Chem Soc. 1977;99:5215.
- Moskovits M. Surface roughness and the enhanced intensity of Raman scattering by molecules adsorbed on metals. J Chem Phys 1978;69:4159.
- Gersten JI, Nitzan A. Electromagnetic theory of enhanced Raman scattering by molecules adsorbed on rough surfaces. J Chem Phys. 1980;73:3023.
- Gersten JI. The effect of surface roughness on surface enhanced Raman scattering. J Chem Phys. 1980;72:5779.
- Gersten JI. Rayleigh, Mie, and Raman scattering by molecules adsorbed on rough surfaces. J Chem Phys. 1980; 72:5780.
- McCall SL, Platzman PM, Wolff PA. Surface enhanced Raman scattering. Phys Lett A. 1980;77:381.
- Kerker M, Wang DS, Chew H. Surface enhanced Raman scattering (SERS) by molecules adsorbed at spherical particles: errata. Appl Opt. 1980;19:4159.
- Gersten JI, Nitzan A. Spectroscopic properties of molecules interacting with small dielectric particles. J Chem Phys. 1980;75:1139.
- Willetts KA, Van Duyne RP. Localized surface plasmon resonance spectroscopy and sensing. Annu Rev Phys Chem. 2007;58:267.
- Otto A, Mrozek I, Grabhorn H, Akemann W. Surface-enhanced Raman scattering. J Phys: Condens Matter. 1992;4:1143.
- Kneipp K, Wang Y, Kneipp H, Perelman LT, Itzkan I, Dasari RR, Feld MS. Single molecule detection using surface-enhanced Raman scattering (SERS). Phys Rev Lett 1997;78:1667.
- Nie S, Emory SR. Probing single molecules and single nanoparticles by surface-enhanced Raman scattering. Science. 1997;275:1102.
- Xu H, Bjerneld EJ, Käll M, Börjesson L. Spectroscopy of single hemoglobin molecules by surface enhanced Raman Scattering. Phys Rev Lett. 1999;83:4357.
- Bjerner EJ, Johansson P, Käll M. Single molecule vibrational fine-structure of tyrosine adsorbed on Ag nanocrystals. Single Mol. 2000;1:239.

40. Weiss A, Haran G. Time-dependent single-molecule Raman scattering as a probe of surface dynamics. *J Phys Chem.* 2001;105:12348.
41. Dieringer J, Lettan R, Scheidt K, Van Duyne R. A frequency domain existence proof of single-molecule surface-enhanced Raman spectroscopy. *J Am Chem Soc.* 2007;129:16249.
42. Michaels AM, Jiang J, Brus L. Ag nanocrystal junctions as the site for surface-enhanced Raman Scattering of single rhodamine 6G molecules. *J Phys Chem B.* 2000;104:11965.
43. Xu H, Aizpurua J, Käll M, Apell P. Electromagnetic contributions to single-molecule sensitivity in surface-enhanced Raman scattering. *Phys Rev E.* 2000;62:4318.
44. Kneipp K, Kneipp H, Itzkan I, Dasari RR, Feld MS. Ultra-sensitive chemical analysis by Raman spectroscopy. *Chem Rev.* 1999;99:2957.
45. Haynes C, Yonzon C, Zhang X, Van Duyne R. Surface-enhanced Raman sensors: early history and the development of sensors for quantitative biowarfare agent and glucose detection. *J Raman Spectrosc.* 2005;36:471.
46. Aravind PK, Rendel RW, Metiu H. A new geometry for field enhancement in surface-enhanced spectroscopy. *Chem Phys Lett.* 1982;85:396.
47. Zenhausern F, O'Boyle MP, Wickramasinghe HK. Apertureless near-field optical microscope. *Appl Phys Lett.* 1994;65:1623.
48. Inouye Y, Kawata S. Near-field scanning optical microscope with a metallic probe tip. *Opt Lett.* 1994;19:159.
49. Wessel J. Surface-enhanced optical microscopy. *J Opt Soc Am B.* 1985;2:1538.
50. Fischer UC, Pohl DW. Observation of single-particle plasmons by near-field optical spectroscopy. *Phys Rev Lett.* 1989;62:458.
51. Specht M, Pedarnig JD, Heckl WM, Hänsch TW. Scanning plasmon near-field microscopy. *Phys Rev Lett.* 1992;68:477.
52. Bachelot R, Gleyzes P, Boccara AC. Near-field optical microscope based on local perturbation of a diffraction spot. *Opt Lett.* 1995;20:1924.
53. Koglin J, Fischer UC, Fuchs H. Material contrast in scanning near-field optical microscopy at 1–10 nm resolution. *Phys Rev B.* 1997;55:7977.
54. Sánchez EJ, Novotny L, Xie XS. Near-field fluorescence microscopy on two-photon excitation with metal tips. *Phys Rev Lett.* 1999;82:4014.
55. Keilmann F, van der Weide DW, Eickelkamp T, Merz R, Stockle D. Extreme sub-wavelength resolution with a scanning radio-frequency transmission microscope. *Opt Commun.* 1996;129:15.
56. Knoll B, Keilmann F. Near-field probing of vibrational absorption for chemical microscopy. *Nature.* 1999;399:134.
57. Knoll B, Keilmann F. Enhanced dielectric contrast in scattering-type scanning near-field optical microscopy. *Opt Commun.* 2000;182:321.
58. Raschke MB, Molina L, Elsaesser T, Kim DH, Knoll W, Hinrichs K. Apertureless near-field vibrational imaging of block-copolymer nanostructures with ultrahigh spatial resolution. *ChemPhysChem.* 2005;6:2197.
59. ad V Shalaev SK, editor. Tip enhancement. In: *Advances in nano-optics and nano-photonics.* Amsterdam: Elsevier; 2007.
60. Kneipp K, Moskovits M, Kneipp H, editors. *Surface-Enhanced Raman scattering: physics and applications. Topics in applied physics.* Berlin: Springer; 2006.
61. Rasmussen A, Deckert V. New dimension in nano-imaging: breaking through the diffraction limit with scanning near-field optical microscopy. *Anal Bioanal Chem.* 2005;381:165.
62. Novotny L. The history of near-field optics. *Progr Opt.* 2007;50:137.
63. Krug II JT, Sánchez EJ, Xie XS. Design of near-field optical probes with optimal field enhancement by finite difference time domain electromagnetic simulation. *J Chem Phys.* 2002;116:10895.
64. Richards D, Milner RG, Huang F, Festy F. Tip-enhanced Raman microscopy: practicalities and limitations. *J Raman Spectrosc.* 2003;34:663.
65. Kawata S. *Near-field optics and surface plasmon polaritons.* Berlin: Springer; 2001.
66. Stoockle RM, Suh YD, Deckert V, Zenobi R. Nanoscale chemical analysis by tip-enhanced Raman spectroscopy. *Chem Phys Lett.* 2000;318:131.
67. Anderson MS. Locally enhanced Raman spectroscopy with an atomic force microscope. *Appl Phys Lett.* 2000;76:3130.
68. Hayazawa N, Inouye Y, Sekkat Z, Kawata S. Metallized tip amplification of near-field Raman scattering. *Opt Commun.* 2000;183:333.
69. Hayazawa N, Inouye Y, Sekkat Z, Kawata S. Near-field Raman scattering enhanced by a metallized tip. *Chem Phys Lett.* 2001;335:369.
70. Hayazawa N, Inouye Y, Sekkat Z, Kawata S. Near-field Raman imaging of organic molecules by an apertureless metallic probe scanning optical microscope. *J Chem Phys.* 2002;117:1296.
71. Anderson MS, Pike WT. A Raman-atomic force microscope for apertureless-near-field spectroscopy and optical trapping. *Rev Sci Instrum.* 2002;73:1198.
72. Hartschuh A, Anderson N, Novotny L. Near-field Raman spectroscopy using a sharp metal tip. *J Microscop.* 2002; 210:234.
73. Hartschuh A, Sánchez EJ, Xie XS, Novotny L. High-resolution near-field Raman microscopy of single-walled carbon nanotubes. *Phys Rev Lett.* 2003;90:095503.
74. Watanabe H, Ishida Y, Hayazawa N, Inouye Y, Kawata S. Tip-enhanced near-field Raman analysis of tip-pressurized adenine molecule. *Phys Rev B.* 2004;69:155418.
75. Ichimura T, Hayazawa N, Hashimoto M, Inouye Y, Kawata S. Tip-enhanced coherent anti-Stokes Raman scattering for vibrational nanoimaging. *Phys Rev Lett.* 2004; 92:220801.
76. Hayazawa N, Ichimura T, Hashimoto M, Inouye Y, Kawata S. Amplification of coherent anti-Stokes Raman scattering by a metallic nanostructure for a high resolution vibration microscopy. *J Appl Phys.* 2004;95:2676.
77. Pettinger B, Ren B, Picardi G, Schuster R, Ertl G. Tip-enhanced Raman spectroscopy (TERS) of malachite green isothiocyanate at Au(111): bleaching behavior under the influence of high electromagnetic fields. *J Raman Spectrosc.* 2005;36:541.
78. Anderson N, Hartschuh A, Cronin S, Novotny L. Nanoscale vibrational analysis of single-walled carbon nanotubes. *J Am Chem Soc.* 2005;127:2533.
79. Domke K, Zhang D, Pettinger B. Toward Raman fingerprints of single dye molecules at atomically smooth Au(111). *J Am Chem Soc.* 2006;128:14721.
80. Verma P, Yamada K, Watanabe H, Inouye Y, Kawata S. Near-field Raman scattering investigation of tip effects on C60 molecules. *Phys Rev B.* 2006;73:145416.
81. Neacsu CC, Dreyer J, Behr N, Raschke MB. Scanning-probe Raman spectroscopy with single-molecule sensitivity. *Phys Rev B.* 2006;73:193406.
82. Steidtner J, Pettinger B. High-resolution microscope for tip-enhanced optical processes in ultrahigh vacuum. *Rev Sci Instr.* 2007;78:103104.

83. Hayazawa N, Watanabe H, Saito Y, Kawata S. Towards atomic site-selective sensitivity in tip-enhanced Raman spectroscopy. *J Chem Phys.* 2006;125:244706.
84. Neugebauer U, Roesch P, Schmitt M, Popp J, Julien C, Rasmussen A, Budich C, Deckert V. On the way to nanometer-sized information of the bacterial surface by tip-enhanced Raman spectroscopy. *ChemPhysChem.* 2006; 7:1428.
85. Zhang W, Yeo BS, Schmid T, Zenobi R. Single molecule tip-enhanced Raman spectroscopy with silver tips. *J Phys Chem C.* 2007;111:1733.
86. Jersch J, Demming F, Hildenhagen L, Dickmann K. Field enhancement of optical radiation in the nearfield of scanning probe microscope tips. *Appl Phys A.* 1998;66:29.
87. Demming F, Jersch J, Dickmann K, Geshev PI. Calculation of the field enhancement on laser-illuminated scanning probe tips by the boundary element method. *Appl Phys B.* 1998;66:593.
88. Klein S, Witting T, Dickmann K, Geshev P, Hietschold M. On the field enhancement at laser-illuminated scanning probe tips. *Single Mol.* 2002;3:281.
89. Mills DL. Theory of STM-induced enhancement of dynamic dipole moments on crystal surfaces. *Phys Rev B.* 2002;65:125419.
90. Wu S, Mills DL. STM-induced enhancement of dynamic dipole moments on crystal surfaces: Theory of the lateral resolution. *Phys Rev B.* 2002;65:205420.
91. Micic M, Klymyshyn N, Suh YD, Lu HP. Finite element method simulation of the field distribution for AFM tip-enhanced surface-enhanced Raman scanning microscopy. *J Phys Chem.* 2003;107:1574.
92. Neacsu CC, Reider GA, Raschke MB. Second-harmonic generation from nanoscopic metal tips: Symmetry selection rules for single asymmetric nanostructures. *Phys Rev B.* 2005;71(20):201402.
93. Neacsu CC, Steudle GA, Raschke MB. Plasmonic light scattering from nanoscopic metal tips. *Appl Phys B.* 2005; 80(3):295.
94. Roth RM, Panoiu NC, Adams MM, Osgood RM, Neacsu CC, Raschke MB. Resonant-plasmon field enhancement from asymmetrically illuminated conical metallic-probe tips. *Opt Expr.* 2006;14:2921.
95. Behr N, Raschke M. Optical antenna properties of scanning probe tips: plasmonic light scattering, tip-sample coupling, and near-field enhancement. *J Phys Chem C.* 2008;112:3766.
96. Neacsu CC, Dreyer J, Behr N, Raschke MB. Reply to "Comment on 'Scanning-probe Raman spectroscopy with single-molecule sensitivity'". *Phys Rev B.* 2007;75:236402.
97. Anderson N, Anger P, Hartschuh A, Novotny L. Subsurface raman imaging with nanoscale resolution. *Nano Lett.* 2006;6(4):744.
98. Debus C, Lieb A, Drechsler A, Meixner AJ. Probing highly confined optical field in the focal region of a high NA parabolic mirror with subwavelength spatial resolution. *J Microsc.* 2002;210:203.
99. Anger P, Feltz A, Berghaus T, Meixner AJ. Near-field and confocal surface-enhanced resonance Raman spectroscopy at cryogenic temperatures. *J Microsc.* 2003;209:162.
100. Novotny L, Sánchez EJ, Xie XS. Near-field optical imaging using metal tips illuminated by higher-order Hermite-Gaussian beams. *Ultramicroscopy.* 1998;71:21.
101. Novotny L, Beversluis MR, Youngworth KS, Brown TG. Longitudinal field modes probed by single molecules. *Phys Rev Lett.* 2001;86(23):5251-4.
102. Karrai K, Tiemann I. Interfacial shear force microscopy. *Phys Rev B.* 2000;62:13174.
103. Stipe BC, Mamin HJ, Stowe TD, Kenny TW, Rugar D. Noncontact friction and force fluctuations between closely spaced bodies. *Phys Rev Lett.* 2001;87:096801.
104. Gregor MJ, Blome PG, Schafer J, Ulbrich RG. Probe-surface interaction in near-field optical microscopy: The nonlinear bending force mechanism. *Appl Phys Lett.* 1996; 68:307.
105. Williamson RL, Brereton LJ, Antognozzi M, Miles MJ. Are artefacts in scanning near-field optical microscopy related to the misuse of shear force? *Ultramicroscopy.* 1998; 71:165.
106. Hoppe S, Ctistis G, Paggel JJ, Fumagalli P. Spectroscopy of the shear force interaction in scanning near-field optical microscopy. *Ultramicroscopy.* 2005;102:221.
107. Karrai K, Grober RD. Piezoelectric tip sample distance control for near field optical microscopes. *Appl Phys Lett.* 1995;66:1842.
108. Davy S, Spajer M, Courjon D. Influence of the water layer on the shear force damping in near-field microscopy. *Appl Phys Lett.* 1998;73:2594.
109. Okajima T, Hirotsu S. Study of probe-surface interaction in shear-force microscopy: effects of humidity and lateral spring constant. *Opt Rev.* 1998;5:303.
110. Durkan C, Shvets IV. Investigation of the physical mechanisms of shear-force imaging. *J Appl Phys.* 1996;80:5659.
111. Bernstein HJ, Buckingham AD. Resonance Raman spectra [and Discussion]. *Phil Trans R Soc London A, Math Phys Sci.* 1979;293:287.
112. Pettinger B, Ren B, Picardi G, Schuster R, Ertl G. Nanoscale probing of adsorbed species by tip-enhanced Raman spectroscopy. *Phys Rev Lett.* 2004;92:096101.
113. Guckenberger R, Hartmann T, Wiegand W, Bauneister W. *Scanning tunneling microscopy II.* New York: Springer; 1995.
114. Ibe J, Bey JP, Brandow S, Brizzolara R, Burnham N, Dilella D, Lee K, Marrian C, Colton R. On the electrochemical etching of tips for scanning tunneling microscopy. *J Vac Sci Technol A.* 1990;8:3570.
115. Vasile MJ, Grigg DA, Griffith JE, Fitzgerald EA, Russell PE. Scanning probe tips formed by focused ion beams. *Rev Sci Instr.* 1991;62:2167.
116. Nam AJ, Teren A, Lusby TA, Melmed AJ. Benign making of sharp tips for STM and FIM: Pt, Ir, Au, Pd, and Rh. *J Vac Sci Technol B.* 1995;13:1556.
117. Iwami M, Uehara Y, Ushioda S. Preparation of silver tips for scanning tunneling microscopy imaging. *Rev Sci Instr.* 1998;69:4010.
118. Ichimura T, Watanabe H, Morita Y, Verma P, Kawata S, Inouye Y. Temporal fluctuation of tip-enhanced Raman spectra of adenine molecules. *J Phys Chem C.* 2007; 111(26):9460-4.
119. Ossikovski R, Nguyen Q, Picardi G. Simple model for the polarization effects in tip-enhanced Raman spectroscopy. *Phys Rev B.* 2007;75:045412.
120. Kuhn S, Hkanson U, Rogobete L, Sandoghdar V. Enhancement of single-molecule fluorescence using a gold nanoparticle as an optical nanoantenna. *Phys Rev Lett.* 2006;97:017402.
121. Ren B, Picardi G, Pettinger B. Preparation of gold tips suitable for tip-enhanced Raman spectroscopy and light emission by electrochemical etching. *Rev Sci Instr.* 2004; 75:837.
122. Picardi G, Nguyen Q, Schreiber J, Ossikovski R. Comparative study of atomic force mode and tunneling mode tip-enhanced Raman spectroscopy. *Eur Phys J App Phys.* 2007;40:197.

123. Klein M, Schwitzgebel G. An improved lamellae drop-off technique for sharp tip preparation in scanning tunneling microscopy. *Rev Sci Instr.* 1997;68:3099.
124. Wang X, Liu Z, Zhuang MD, Zhang HM, Wang X, Xie ZX, Wu DY, Ren B, Tian ZQ. Tip-enhanced Raman spectroscopy for investigating adsorbed species on a single-crystal surface using electrochemically prepared Au tips. *App Phys Lett.* 2007;91:101105.
125. Melmed A. The art and science and other aspects of making sharp tips. *J Vac Sci Technol B.* 1990;9:601.
126. Frankenthal RP, Thompson DE. The anodic behavior of Gold in sulfuric acid solutions. *J Electrochem Soc.* 1976;123:799.
127. Mao BW, Ren B, Cai XW, Xiong LH. Electrochemical oscillatory behavior under a scanning electrochemical microscopic configuration. *J Electroanal Chem.* 1995;394:155.
128. Hillier J. On the investigation of specimen contamination in the electron microscope. *J App Phys.* 1947;19:226.
129. Guise O, Ahner J, Yates J, Levy J. Formation and thermal stability of sub-10-nm carbon templates on Si(100). *App Phys Lett.* 2004;85:2352.
130. Denk W, Pohl DW. Near-field optics: microscopy with nanometer-size fields. *J Vac Sci Technol B.* 1991;9:510.
131. Novotny L, Bian RX, Xie XS. Theory of nanometric optical tweezers. *Phys Rev Lett.* 1997;79:645.
132. Porto JA, Johansson P, Apell SP, Lopez-Rios T. Resonance shift effects in apertureless scanning near-field optical microscopy. *Phys Rev B.* 2003;67:085409.
133. Bohren C, Huffman D. Absorption and scattering of light by small particles. New York: Wiley; 1998.
134. Kretschmann E. Untersuchungen zur anregung und Streuung von Oberflaechenplasmaschwingungen an Silberschichten. PhD thesis, University Hamburg; 1972.
135. Leurgans P, Turner AF. Frustrated total internal reflection interference filters. *J Opt Soc Am.* 1947;37:983.
136. Heinz TF, Loy MMT, Thompson WA. Study of Si(111) surfaces by optical second-harmonic generation: reconstruction and surface phase transformation. *Phys Rev Lett.* 1985;54:63.
137. Boyd RW. Nonlinear optics. 2nd ed. London: Academic; 2003.
138. Ropers C, Neacsu CC, Raschke MB, Albrecht M, Lienau C, Elsaesser T. Light confinement at ultrasharp metallic tips. *Jpn J Appl Phys.* 2008;47:6051.
139. Bouhelier A, Renger J, Beversluis MR, Novotny L. Plasmon-coupled tip-enhanced near-field optical microscopy. *J Microsc.* 2003;210:220.
140. Festy F, Demming A, Richards D. Resonant excitation of tip plasmons for tip-enhanced Raman SNOM. *Ultramicroscopy.* 2004;100:437.
141. Schneider SC, Grafstroem S, Eng LM. Scattering near-field optical microscopy of optically anisotropic systems. *Phys Rev B.* 2005;71:115418.
142. Goncharenko AV, Dvoynenko MM, Chang HC, Wang JK. Electric field enhancement by a nanometer-scaled conical metal tip in the context of scattering-type near-field optical microscopy. *Appl Phys Lett.* 2006;88:104101.
143. Martin YC, Hamann HF, Wickramasinghe HK. Strength of the electric field in apertureless near-field optical microscopy. *J Appl Phys.* 2001;89:5774.
144. Downes A, Salter D, Elflick A. Finite element simulations of tip-enhanced Raman and fluorescence Spectroscopy. *J Phys Chem B.* 2006;110:6692.
145. Stratton JA. Electromagnetic theory. Sydney: Mcgraw-Hill; 1941.
146. Metiu H. Surface enhanced spectroscopy. *Progr Surf Sci.* 1984;17:153.
147. Palik E, editor. Handbook of optical constants of solids. Berlin: Springer; 2000.
148. Demming AL, Festy F, Richards D. Plasmon resonances on metal tips: understanding tip-enhanced Raman scattering. *J Chem Phys.* 2005;122:184716.
149. Jackson JD. Classical electrodynamics. 3rd ed. vol. 1, chapt. 2, New York: Wiley; 1999.
150. Geshev PI, Klein S, Witting T, Dickmann K, Hietschold M. Calculation of the electric-field enhancement at nanoparticles of arbitrary shape in close proximity to a metallic surface. *Phys Rev B.* 2004;70:075402.
151. Aravind PK, Nitzan A, Metiu H. The interaction between electromagnetic resonances and its role in spectroscopic studies of molecules adsorbed on colloidal particles or metal spheres. *Surf Sci.* 1983;110:189.
152. Pettinger B, Domke K, Zhang D, Schuster R, Ertl G. Direct monitoring of plasmon resonances in a tip-surface gap of varying width. *Phys Rev B.* 2007;76:113409.
153. Berndt R, Gimzewski JK, Johansson P. Inelastic tunneling excitation of tip-induced plasmon modes on noble-metal surfaces. *Phys Rev Lett.* 1991;67:4878.
154. Aizpurua J, Apell SP, Berndt R. Role of tip shape in light emission from the scanning tunneling microscope. *Phys Rev B.* 2000;62:2065.
155. Raether H. Surface plasmons on smooth and rough surfaces and on gratings. New York: Springer; 1988.
156. Lueck HB, Daniel DC, McHale JL. Resonance Raman study of solvent effects on a series of triarylmethane dyes. *J Raman Spectrosc.* 1993;24:363.
157. Beversluis MR, Bouhelier A, Novotny L. Continuum generation from single gold nanostructures through near-field mediated intraband transitions. *Phys Rev B.* 2003;68:115433.
158. Moskovits M. Surface-enhanced spectroscopy. *Rev Mod Opt.* 1985;57:783.
159. Haes AJ, Haynes CL, McFarland AD, Schatz GC, Van Duyne RP, Zou S. Plasmonic materials for surface-enhanced sensing and spectroscopy. *MRS Bull.* 2005;30:368.
160. McFarland AD, Young MA, Dieringer JA, Van Duyne RP. Wavelength-scanned surface-enhanced raman excitation spectroscopy. *J Phys Chem B.* 2005;109:11279.
161. Aravind PK, Metiu H. The effects of the interaction between resonances in the electromagnetic response of a sphere-plane structure: applications to surface enhanced spectroscopy. *Surf Sci.* 1983;124:506.
162. Fowles R. Introduction to modern optics. 2nd ed. Holt: Rinehart & Winston; 1975.
163. Lee KG, Kihm HW, Kihm JE, Choi WJ, Kim H, Ropers C, Park DJ, Yoon YC, Choi SB, Woo DH, Kim J, Lee B, Park QH, Lienau C, Kim DS. Vector field microscopic imaging of light. *Nat Photon.* 2006;1:53.
164. Gersen H, Novotny L, Kuipers L, van Hulst NF. On the concept of imaging nanoscale vector fields. *Nat Photon.* 2007;1:242.
165. Lee KG, Kihm HW, Kihm JE, Choi WJ, Kim H, Ropers C, Park DJ, Yoon YC, Choi SB, Woo DH, Kim J, Lee B, Park QH, Lienau C, Kim DS. On the concept of imaging nanoscale vector fields. *Nat Photon.* 2007;1:243.
166. Poborchii V, Tada T, Kanayama T. Subwavelength-resolution Raman microscopy of Si structures using metal-particle-topped AFM probes. *Jpn J Appl Phys.* 2005;44:202.
167. Schneider S, Brehm G, Freunshcht P. Comparison of surface-enhanced Raman and hyper-Raman spectra of the triph-

- enylmethane dyes crystal violet and malachite green. *Phys Stat Sol B*. 1995;189:37.
168. Polubotko AM. SERS phenomenon as a manifestation of quadrupole interaction of light with molecules. *Phys Lett*. 1990;146:81.
169. Sass JK, Neff H, Moskovits M, Holloway S. Electric field gradient effects on the spectroscopy of adsorbed molecules. *J Phys Chem*. 1981;85:621.
170. Creighton J. Spectroscopy of surfaces. *Advances in spectroscopy*, vol. 16. chap. Selection rules for surface-enhanced raman spectroscopy, 37. New York: Wiley; 1988.
171. Ayars EJ, Hallen HD, Jahncke CL. Electric field gradient effects in Raman spectroscopy. *Phys Rev Lett*. 2000;85:4180.
172. Harris DC, Bertolucci MD. Symmetry and spectroscopy: an introduction to vibrational and electronic spectroscopy. New York: Dover; 1989.
173. Moskovits M. Surface selection rules. *J Chem Phys*. 1982;77:4408.
174. Polubotko AM. Some anomalies of the SERS spectra of symmetrical molecules adsorbed on transition metal substrates: application of the dipole-quadrupole SERS theory. *J Raman Spectr*. 2005;36:522.
175. Erdheim GR, Birke RL, Lombardi JR. Surface enhanced Raman spectrum of pyrazine. Observation of forbidden lines at the electrode surface. *Chem Phys Lett*. 1980;69:495.
176. Dornhaus R, Long MB, Benner RE, Chang RK. Time development of SERS from pyridine, pyrimidine, pyrazine, and cyanide adsorbed on Ag electrodes during an oxidation-reduction cycle. *Surf Sci*. 1980;93:240.
177. Moskovits M, Dilella DP. Enhanced Raman spectra of ethylene and propylene adsorbed on silver. *Chem Phys Lett*. 1980;73:500.
178. Maher RC, Cohen LF, Etchegoin P. Single molecule photo-bleaching observed by surface enhanced resonant Raman scattering (SERRS). *Chem Phys Lett*. 2002;352:378.
179. Wang Z, Rothberg LJ. Origins of blinking in single-molecule Raman spectroscopy. *J Phys Chem*. 2005;109:3387.
180. Xie XS, Trautman JK. Optical studies of single molecules at room temperatures. *Annu Rev Phys Chem*. 1998;49:441.
181. Moyer P, Smith J, Eng L, Meixner A. Surface-Enhanced Raman scattering spectroscopy of single carbon domains on individual Ag nanoparticles on a 25 ms time scale. *J Am Chem Soc*. 2000;122:5409.
182. Kudelski A, Pettinger B. SERS on carbon chain segments: monitoring locally surface chemistry. *Chem Phys Lett*. 2000;321:356.
183. Picardi G. Raman spectroscopy and light emission at metal surfaces enhanced by the optical near-field of a scanning tunneling tips. Ph.D. thesis, Freie Universität Berlin; 2003.
184. Futamata M, Maruyama Y, Ishikawa M. Critical importance of the junction in touching Ag particles for single molecule sensitivity in SERS. *J Molec Struct*. 2005;735:75.
185. Le Ru EC, Etchegoin PG, Meyer M. Enhancement factor distribution around a single SERS hot-spot and its relation to single molecule detection. *J Chem Phys*. 2006;125:204701.
186. Friedrich B, Herschbach D. Alignment and trapping of molecules in intense laser fields. *Phys Rev Lett*. 1995; 74:4623.
187. Steidtner J, Pettinger B. Tip-enhanced Raman spectroscopy and microscopy on single dye molecule with 15 nm resolution. *Phys Rev Lett*. 2008;100:236101.
188. Chien CT, Wu MC, Wei CW, Yang HH, Wu JJ, Su WF, Lin CS, Chen YF. Polarization-dependent confocal Raman microscopy of an individual ZnO nanorod. *App Phys Lett*. 2008;92:223102.
189. Fan HM, Fan XF, Ni ZH, Shen ZX, Feng YP, Zou BS. Orientation-dependent Raman spectroscopy of single wurtzite CdS nanowires. *J Phys Chem C*. 2008;112:1865.
190. Lee N, Hartschuh RD, Mehtani D, Kisliuk A, Maguire JF, Green M, Foster MD, Sokolov AP. High contrast scanning nano-Raman spectroscopy of silicon. *J Raman Spectrosc*. 2007;38:789–96.
191. Nguyen Q, Ossikovski R, Schreiber J. Contrast enhancement on crystalline silicon in polarized reflection mode tip-enhanced Raman spectroscopy. *Sci Direct*. 2007;274:231–5.
192. Saito Y, Motohashi M, Hayazawa N, Iyoki M, S Kawata S. Nanoscale characterization of strained silicon by tip-enhanced Raman spectroscopy in reflection mode. *Appl Phys Lett*. 2006;88:143109.
193. Chen JY, Wiley BJ, Xia YN. One-dimensional nanostructures of metals: large-scale synthesis and some potential applications. *Langmuir*. 2007;23:4120.
194. Zhu Y, Ke C, Espinosa HD. Experimental techniques for the mechanical characterization of one-dimensional nanostructures. *Exp Mech*. 2007;47:7.
195. Wang ZL. New developments in transmission electron microscopy on the nanoscale. *Adv Mat*. 2003;15:1497.
196. Zhang XF, Zhang Z. Progress in transmission electron microscopy 2: applications in materials science (Springer Series in Surface Sciences). New York: Springer; 2001.
197. Zuo JM, Vartanyants I, Gao M, Zhang R, Nagahara LA. Atomic resolution imaging of a carbon nanotube from diffraction intensities. *Science*. 2003;300:1419.
198. Chapman HN, Barty A, Marchesini S, Noy A, Hau-Riege SP, Cui C, Howells MR, Rosen R, He H, Spence JCH, Weierstall U, Beetz T, Jacobsen C, Shapiro D. High-resolution ab initio three dimensional x-ray diffraction microscopy. *J Opt Soc Am A*. 2006;5:1179.
199. M DiDomenico SHW, Porto SPS. Raman spectrum of single-domain BaTiO₃. *Phys Rev*. 1968;174:522–30.
200. Li Z, Foster CM, Dai XH, Xu XZ, Chan SK, Lam DJ. Piezoelectrically-induced switching of 90 degree domains in tetragonal BaTiO₃ and PbTiO₃ investigated by micro-Raman spectroscopy. *J App Phys*. 1992;71(9):4481–6.
201. Nakamura M, Orihara H, Ishibashi Y, Hara K. Observation of ferroelastic domains in LaNbO₄ by micro-Raman spectroscopy. *J Phys Soc Jpn*. 1990;59:4472–5.
202. Gardiner DJ. Practical Raman spectroscopy. New York: Springer; 1989.
203. Drago RS. Physical methods for chemists. Surfside Scientific Publishers; 1992.
204. C A Arguello DL, Porto SPS. First-order raman effect in wurtzite-type crystals. *Phys Rev*. 1969;181:1351.
205. Moerland RJ, Taminiau TH, Novotny L, van Hulst NF, Kuipers L. Reversible polarization control of single photon emission. *Nano Lett*. 2008;8:606–10.
206. Ayars E, Jahncke C, Paesler M, Hallen H. Fundamental differences between micro- and nano-Raman spectroscopy. *J Microsc*. 2001;202:142.
207. Ropers C, Neacsu CC, Elsaesser T, Albrecht M, Raschke MB, Lienau C. Grating-coupling of surface plasmons onto metallic tips: a nanoconfined light source. *Nano Lett*. 2007;7:2784. (Featured in: *Nature Photonics* 446:500).
208. Stockman MI, Bergman DJ, Anceau C, Brasselet S, Zyss J. Enhanced second-harmonic generation by metal surfaces with nanoscale roughness: nanoscale dephasing, depolarization, and correlations. *Phys Rev Lett*. 2004;92:057402.
209. Ebbesen TW, Lezec HJ, Ghaemi HF, Thio T, Wolff PA. Extraordinary optical transmission through sub-wavelength hole arrays. *Nature*. 1998;391:667.